SIMULATION OF METAL HALIDE ELECTRIC DISCHARGE LAMPS USING FINITE VOLUME TECHNIQUES

BY

BRIAN MICHAEL LAY

B.E.E., University of Minnesota, 1998

THESIS

Submitted in partial fulfillment of the requirements
for the degree of Master of Science in Electrical Engineering
in the Graduate College of the
University of Illinois at Urbana-Champaign, 2000

Urbana, Illinois

(INSERT SIGNITURE PAGE HERE)

SIMULATION OF METAL HALIDE ELECTRIC DISCHARGE LAMPS USING FINITE VOLUME TECHNIQUES

Brian Michael Lay
Department of Electrical and Computer Engineering
University of Illinois at Urbana-Champaign, 2000
Mark J. Kushner, Advisor

Metal halide lamps are becoming popular for a variety of commercial and residential applications. In this work we computationally study the dynamics of high-pressure metal halide lamps during the early stages of their ignition. The sputtering that occurs during the ignition process has important implications on the lifetime and transparency of the lamp. The goal of this thesis is to develop a model that is capable of capturing the complex geometry and plasma properties of an actual metal halide lamp.

This thesis includes two parametric studies. The first varies the voltage across the lamp, the secondary electron emission coefficients of the electrodes, and the pressure in the lamp to determine their influence on the plasma properties. The second study involves placing a starter probe in the arc tube as a second source of ionization. By pre-ionizing the gas in the lamp, the sputtering during the starting process can be minimized. The model was able to demonstrate this effect.

ACKNOWLEDGMENTS

I would like to take this opportunity to thank my advisor, Professor Mark J. Kushner, for his guidance and encouragement throughout this work. He has taught me a tremendous amount professionally, concerning all the details of plasma modeling, as well as personally in our many informal conversations. This work would not have been possible without his insight and dedication.

I would also like to thank all my fellow group members. Rajesh Dorai, Pramod Subramonium, and Arvind Sankaran, thank you for all the interesting conversations. Special thanks to Pramod and Arvind for the all the lost hours playing chess that extended my thesis by at least a month. Thank you, Ron Kinder, for clarifying many important technical points and keeping track of the statistics. Da Zhang, Junqing Lu and Dan Cronin, my roommates, deserve credit for tolerating my spontaneous outbursts and indulging them. Thank you, Khaled Hassouni, for the many helpful comments and suggestions when the program had difficulty converging. I must also thank the group members who have since left, Xudong "Peter" Xu, Trudy van der Straaten, and Shahid Rauf, for all of your contributions. To complete the list I must also include Kelly Collier and Gary Eden for all your friendly greetings. I will cherish the memories that this group has given me for many years to come.

Finally, I must thank my family for all their support throughout my college career. My parents have always been there for me. From the beginning they told me that I could do whatever I wanted and they would be proud. They gave me the tools and the confidence to succeed, and for that I will always be indebted. My brother, Chris, and my sister-in-law Jennie, thank you for all the ski trips and more importantly the friendship you have given me, I will

always look up to you. Finally, to my grandparents, uncles, aunts, and cousins, thank you for teaching me to enjoy the finer things in life.

TABLE OF CONTENTS

1. INTRODUCTION 1

   1.1. Applications and Specifications 1
   1.2. Starting Metal Halide Lamps 2
   1.3. Research Involving Metal Halide Lamps 4
   1.4. Overview of the Simulations 7
   1.5. References 10

2. DESCRIPTION OF THE MODEL 12

   2.1. Plasma Solid Simulator Model 12
   2.2. Finite Volume Technique on Triangular Meshes 15
   2.3. Geometry Computations 17
   2.4. Interpolation of *E/N* 19
   2.5. Gas Chemistry 20
   2.6. Solution Technique 22
   2.7. Limitations of the Model 24
   2.8. References 30

3. SIMULATION OF METAL HALIDE LAMPS 31

   3.1. Introduction 31
   3.2. Lamp Geometry 31
   3.3. Base Case 32
   3.4. The Effect of Changing Parameters on the Base Case 34
   3.5. Effect of the Starter on Lamp Operation 36

4. CONCLUSIONS 53

1. INTRODUCTION

1.1 Applications and Specifications

Metal halide lamps are a popular choice for indoor and outdoor lighting applications. These lamps are typically found in streetlights, sporting complexes, factories, gymnasiums, billboards, and storefronts. With the development of new low wattage lamps, applications have expanded to include retail display cases, backlights for rear projection televisions, and an array of indoor lighting applications. A typical metal halide lamp is shown in Figure 1.1 (All figures and tables appear at the end of the chapter). The marketability of metal halide lamps benefits from their high efficiencies, large color rendering indices (CRI) and long lifetimes.

Metal halide lamps are nearly two times more efficient than mercury lamps and typically six to seven times more efficient then incandescent lamps. Efficiency is measured by dividing the light output by the electrical power supplied to the lamp. A typical incandescent lamp has an efficiency around 12 lumens/W, a mercury lamp has an efficiency near 55 lumens/W, while a metal halide lamp can achieve over 90 lumens/W [1]. Higher efficiency translates to fewer lamps and lower electric bills.

The second advantage of metal halide lamps is their high CRI. CRI is a measure of the light quality and is rated on a scale from 0 to 100, with 100 being natural daylight. Metal halide lamps have achieved CRIs in the range of 60 to 80 while mercury vapor lamps tend to fall in the low 20s and incandescent lamps are even lower [1]. Another way to measure the light quality is by its correlated color temperature (CCT). This is a method used to quantify the blackbody radiation from a light source and is measured in Kelvin. A good analogy for understanding this rating is the color transitions that occur in metals as they are heated. At first the metal will be

red-hot, as it is heated further it will become white-hot, and if it heated even further, it will become blue-hot. Yellowish white light has a CCT of 3400 K, bright white light is 3600 K, and daylight is 5500 K. On average, metal halide lamps have a CCT of 4000 K and mercury lamps are in the range of 5600 K. Although mercury lamps have CCTs closer to daylight, their efficiency and CRI are difficult to improve.

Metal halide lamps also have long lifetimes. While operating continuously, metal halide lamps can operate for 15 000 to 20 000 hours. This number can be reduced by cyclic operation or dimming, which will be explained later. Mercury lamps have slightly higher lifetimes on the order of 25 000 hours while incandescent bulbs rarely exceed 1500 hours [1]. Again, this is a compelling reason to shift to high-intensity discharge (HID) metal halide lamps.

The popularity of HID lamps has bolstered the research into improving their operation. The purpose of this thesis is to describe a model that can capture the dynamics of a metal halide lamp as it starts. To support the material in the remainder of this thesis, a description of the starting process is presented in Section 1.2. Section 1.3 describes the research that has been performed on metal halide lamps. Finally, Section 1.4 outlines the remainder of this thesis.

1.2 Starting Metal Halide Lamps

The starting process of metal halide lamps has been studied extensively [2-6] with the intent to improve various aspects of the process. The ignition process has typically been split into five separate stages: breakdown, cold cathode phase, glow discharge phase, glow-to-arc transition, and thermionic arc phase. Each of these phases is described below.

The gas in the arc tube breaks down once the electric fields in the lamp exceed the threshold of the gas. Typically, the ignition process of a metal halide lamp begins with a high

voltage pulse to initiate the ionization process in the tube. The actual breakdown is statistical in nature [6] and can be divided into two parts: the formative lag time and the statistical lag time. The formative lag time is a function of the gas and the *E/N* (electric field / gas number density) values in the tube. This is usually short compared to the statistical lag time, which depends on the availability of free electrons in the arc tube to initiate avalanche.

Following breakdown the lamp either enters a cold cathode discharge phase or a glow discharge phase. If mercury is present on the electrodes, then the lamp enters the cold cathode phase. During this phase, the ions, accelerated by the large electric fields near the electrodes, vaporize the mercury and then ionize it via electron impact ionizations. This in turn decreases the impedance of the lamp since the ionized mercury provides a means of current flow through the lamp. The decrease in impedance is only temporary, though, because the source of mercury is quickly depleted.

The glow discharge phase follows the breakdown of the gas [7]. After the mercury from the electrodes is completely ionized, the impedance of the lamp increases due to the limited availability of charged particles. The primary source of electrons during this period is secondary emissions from the electrodes. Although little is happening in the bulk plasma at this time, the ions bombarding the electrodes deposit their power and slowly begin to heat the tungsten electrodes.

Once the power deposited on the electrodes exceeds a threshold value, the glow-to-arc transition occurs [8, 9]. At this point, the electrodes are so hot that they begin to thermally emit electrons. The thermionic source dominates all other source terms during this phase of lamp ignition, and an arc develops. The conductive path between the electrodes causes the lamp

impedance to fall again. The arc usually takes between 0.5 and 4 minutes to fully develop. The impedance curve for the lamp from breakdown to thermionic emission is shown in Figure 1.2.

1.3 Research Involving Metal Halide Lamps

Despite the success of metal halide lamps in the marketplace, there are still several improvements that can be made to these devices. Most research has concentrated on methods to reduce transparency loss in the arc tube, decrease ignition time, improve the CRI, and investigate the consequences of cyclic operation.

Arc tube darkening is a serious problem in metal halide lamps [10]. Gregor et al. [5] identified three causes of tube darkening via spectroscopic measurements. During the cold cathode phase, ionized mercury from the electrodes condenses on the cool walls. This leads to a temporary transparency loss until the mercury is re-vaporized as the wall temperature increases in the thermionic arc phase. During the glow discharge phase, the large electric fields that develop near the electrodes enhance electrode sputtering. The sputtering results in permanent transparency loss since the tungsten re-deposits on the arc tube walls. Electronic ballasts [11] may help alleviate this problem by carefully regulating the voltage across the discharge, but sputtering still remains the primary cause of lamp darkening. The last source for lamp darkening that Gregor et al. [5] identified was attributed to thermionic emission of tungsten from the electrode. Even if the lamp is operated continuously, such that the sputtering events are minimized, the high temperatures in the lamp will vaporize a small amount of tungsten from the electrodes. Over the life of the lamp this will contribute to lamp darkening as well.

It is beneficial to hasten the ignition process in a metal halide lamp to reduce electrode sputtering. To achieve this goal, early versions of metal halide lamps included a small starter

probe located next to one of the main electrodes. By applying a small voltage between the main electrode and the starter probe, the gas within the arc tube could be pre-ionized. This in turn would permit smaller voltages to be applied between the two main electrodes and still ensure breakdown. Smaller voltages accelerate the ions to lower energies, thereby minimizing electrode sputtering. As the lamps have evolved, the starter probe was removed because it increased the arc tube diameter and provided an undesirable heat sink.

More recently, a small UV starter [2, 3] has been positioned within the glass shroud that encloses the lamp. The UV source produces free electrons by either photoemission from the cathode, photorelease of electrons from the quartz surface, or photoionization. This serves the same purpose as the starter probe, but does not interfere with the dynamics of the arc tube. Byszewski and Budinger [3] performed a statistical study by measuring the time it takes for lamps to breakdown with and without the addition of a UV enhancer. The addition of a UV enhancer dramatically reduced the statistical lag time by providing an external source of free electrons. Zaslavsky et al. [2] performed a similar study to demonstrate another version of a UV enhancer.

Many studies have been performed focusing on improving the optical properties of metal halide lamps [12-14]. As the temperature of the arc increases, the metal halides on the wall of the lamp evaporate. The metal halides diffuse to the center of the arc where enough power is available to dissociate them. The free electrons in the bulk plasma excite and ionize the metal atoms. As the excited metal species return to their ground states, they emit photons in the visible spectrum. The cycle is complete when the metal atoms diffuse to the wall where they recombine with the halides. It should be noted that this process also benefits wall darkening. Just as the halides combine with the metals at the wall, they also combine with the tungsten deposited on

the wall surface and thereby provide a means of transport back to the electrode. This process is referred to wall cleaning [15, 16].

The CRI and the CCT of the lamp are determined by the dose contained in the lamp. Typical doses include NaI/TlI/InI/Hg, ScI_3/NaI/Hg, DyI_3/TlI/Hg, and SnI_2/Hg. Iodides are typically used in lamps because they have a higher vapor pressure and decompose at lower temperatures than chlorides or bromides. Bromides have the drawback that they contribute to electrode erosion. Krasko and Keeffe [12] parameterized a typical lamp fill, NaI/ScI_3/CsI, to determine methods to improve the CRI and the CCT of the lamp. They determined that the addition of LiI filled a void in the spectrum improving the CRI from 65 to 76. The CRI did not show much fluctuation over 8000 hours of continuous operation. Fromm [13] measured several properties of Na/Sc lamps with I/Br halogenides and determined that with a thicker quartz-glass wall, higher dosing quantities, and an electronic ballast, high CCTs and CRIs could be achieved with good maintenance over their lifetimes. Because many commercial lamp fills are proprietary it is difficult to obtain information concerning their content.

As metal halide lamps find more applications in the commercial marketplace, the ability to quickly cycle the lamp becomes more important. There are two problems with cycling lamps. Every time the lamp is cycled the electrodes are sputtered during the glow discharge phase. It was shown in [5] that the relative integrated transmittance of a cycled lamp after 1000 hours drops to 68% compared to a continuously burnt lamp that drops to 90%. The second problem arises from the fact that the voltage required to break down a gas increases as the pressure increases. After a metal halide lamp arrives at its steady state operation, the heat generated from the arc and the subsequent evaporation of the metal halides, causes the pressure inside the lamp to increase several orders of magnitude. When a lamp is turned off it takes several minutes until

the lamp cools back to room temperature, the metal halides condense, and the pressure returns to the original lower value. If the lamp is switched back on during this period, the voltage that the ballast supplies to the lamp is not large enough to break down the gas.

Two approaches to solve this problem have been proposed [6]. Electronic ballasts make it is possible to detect the hot reignition phase and thus apply a larger voltage to the lamp to ensure breakdown. Depending on the gas pressure though, this might not be feasible. Lamps that require in excess of 20-30 kV for reignition pose the risk of external arcing. Another approach is to turn the lamp off slowly. By maintaining just enough voltage across the discharge, a conductive path between the two electrodes can be maintained while the lamp is turning off. A full discharge can be restored quickly by simply increasing the ballast to full power. A similar problem arises when lamps are run at reduced levels in order to conserve energy. Dimming metal halide lamps has been studied by Smith and Zhu [17] and Gibson [18].

The ignition process of a metal halide lamp has serious long-term implications concerning tungsten sputtering, lifetime, and CRI of metal halide lamps. This thesis will attempt to model this process with the goal of using the model to assist in the design and optimization of these lamps.

1.4 Overview of the Simulations

The remainder of this thesis will discuss simulations that were performed on metal halide lamps. Chapter 2 presents an in-depth description of the model used for the simulation and the limitations that are associated with it. The most innovative feature of this simulator is its support for unstructured meshes. Chapter 3 details the parameterization study performed on the metal halide lamps and the resulting trends that were observed. Finally, Chapter 4 concludes the thesis

by discussing the problems encountered while writing this program and noting improvements that can be made in the future.

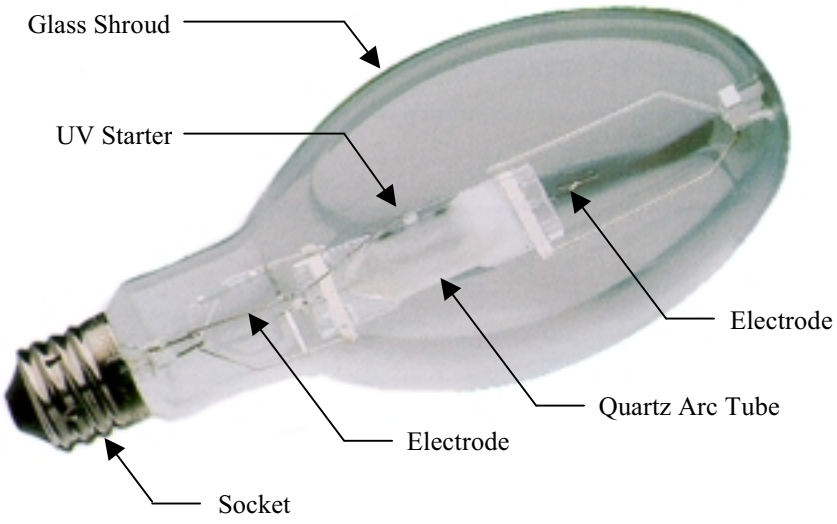

Figure 1.1 Typical metal halide lamp.

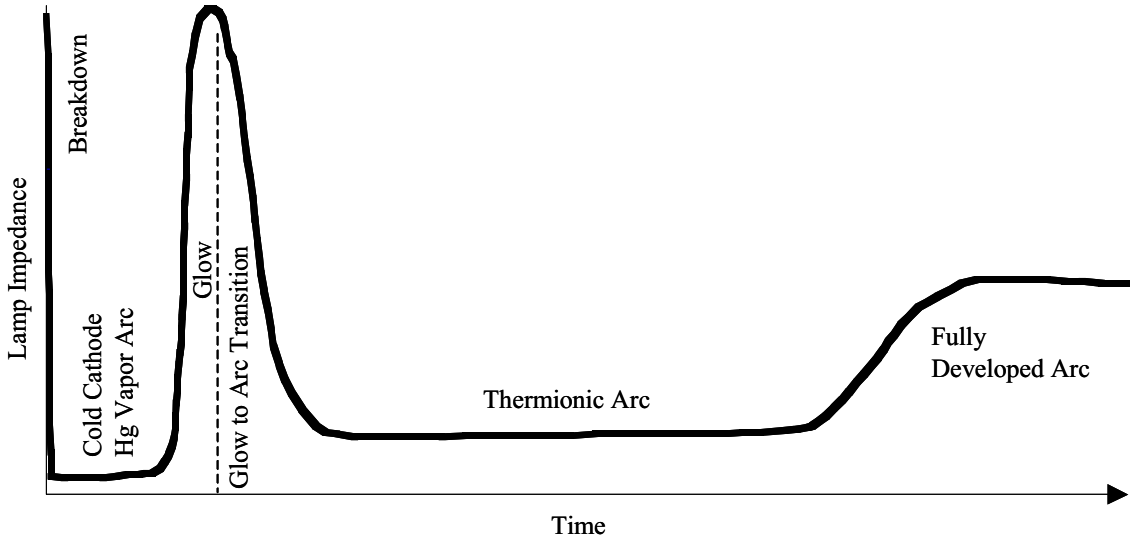

Figure 1.2 HID lamp impedance as a function of time [5].

1.5 References

[1] OSRAM Sylvania, http://www.slyvania.com, product numbers incandescent lamp 11209, mercury lamp 69307, and metal halide lamp 64488.

[2] G. Zaslavsky, S. Cohen, and W. Keeffe, J. Illum. Eng. Soc., **19** (2), 76 (1990).

[3] W. W. Byszewski and A. B. Budinger, J. Illum. Eng. Soc., **19** (2), 70 (1990).

[4] S. Cohen, G. Zaslavsky, and J. N. Lester, J. Illum. Eng. Soc., **18** (2), 3 (1989).

[5] P. D. Gregor, Y. M. Li, A. B. Budinger, and W. W. Byszewski, J. Illum. Eng. Soc., **25** (2), 150 (1996).

[6] W. W. Byszewski, Y. M. Li, A. B. Budinger, and P. D. Gregor, Plasma Sources Sci. Technol., **5**, 720 (1996).

[7] L. C. Pitchford, I. Peres, K. B. Liland, J. P. Boeuf, and H. Gielen, J. Appl. Phys., **82** (1), 112 (1997).

[8] J. F. Waymouth, J. Illum. Eng. Soc., **16** (2), 166 (1987).

[9] G. M. J. F. Luijks and J. A. J. M. van Vliet, Lighting Res. Technol., **20** (3), 87 (1988).

[10] L. Cifuentes, G. M. Forsdyke, and N. W. O'Brien, Corrosion Science, **33** (10), 1581 (1992).

[11] N. Fukumori, H. Nishimura, K. Uchihashi, and M. Fukuhara, J. Illum. Eng. Soc., **24** (1), 41 (1995).

[12] Z. K. Krasko and W. M. Keeffe, J. Illum. Eng. Soc., **19** (1), 118 (1990).

[13] D. C. Fromm, J. Illum. Eng. Soc., **23** (1), 108 (1994).

[14] T. Ozaki and Gin-ya Adachi, J. Appl. Phys., **86** (9), 4723 (1999).

[15] R. J. Campbell, High Temp. Sci., **1**, 303 (1969).

[16] D. M. Speros, R. M. Caldwell and W. E. Smyser, High Temp. Sci., **4**, 99 (1972).

[17] D. Smith and H. Zhu, J. Illum. Eng. Soc., **22** (2), 27 (1993).

[18] R. G. Gibson, J. Illum. Eng. Soc., **23** (2), 19 (1994).

2. DESCRIPTION OF THE MODEL

2.1 Plasma Solid Simulator Model

This chapter describes the algorithms used by the Plasma Solid Simulator (PSS). An overview of the PSS is provided followed by a detailed explanation of each module. The method used here is similar to that of Rauf and Kushner [1] with added support for nonrectilinear meshes. Pitchford et al. [2] and Peres and Pitchford [3] have also applied a similar model to discharge lamps. Emphasis will be placed on the geometrical aspects of this problem because many of the other details can be obtained from the aforementioned sources.

The simulation begins with a description of the lamp. The geometry of the lamp is drawn using an external mesh generator, Computational Fluid Dynamics - Gemetry (CFD-GEOM), and is divided into triangular elements. The shapes in the mesh generator are assigned numbers such that the PSS can associate material properties with the geometries. The output of the mesh generator includes a listing of all the nodes that form the vertices of the triangles, a connectivity list that groups the three nodes that belong to each triangle and the material property number associated with each triangle. This information is used by the PSS to discretize the differential equations.

The heart of the simulation involves solving a coupled set of differential equations at each node in the mesh. Poisson's equation (2.1) is solved to obtain the electric potential distribution across the domain, the species densities are calculated by solving the drift diffusion equations (2.2), and charge accumulation and conduction currents to dielectric surfaces are obtained with a continuity equation (2.3).

$$\nabla \cdot (\varepsilon \nabla \phi) = -\sum_{j=1}^{N_{ch}} q_j n_j - \rho \tag{2.1}$$

$$\frac{\partial n_i}{\partial t} - \nabla \cdot \left(D_i \nabla n_i \pm \mu_i n_i \nabla \phi \right) = S_i \tag{2.2}$$

$$\frac{\partial \rho}{\partial t} = \sum_{j=1}^{N_{ch}} q_j \nabla \cdot \left(D_j \nabla n_j \pm \mu_j n_j \nabla \phi \right) - \nabla \cdot \left(\sigma \left(- \nabla \phi \right) \right) \tag{2.3}$$

where ε, ϕ, q, n, ρ, D, μ, S, and σ are permittivity, electric potential, fundamental charge, number density, charge density, diffusion coefficient, mobility, source function and conductivity of solid materials, respectively. N_{ch} is the total number of charged gas species. The i subscripts in Equations (2.1) and (2.2) refer to charged species. The source function in Equation (2.2) includes the gain and loss terms due to gas phase reactions and contributions associated with secondary electron emission from surfaces.

A block diagram of the simulation is in Figure 2.1. The equations above are linearized at each time step using a conservative finite volume method and are solved implicitly using Newton's method. The Sharfetter-Gummel technique [4, 5] is applied to the drift-diffusion terms in the above equations to allow for larger time steps. This incorporates an upwind/downwind term for the flux associated with the drift term and also takes into account fluxes that are strongly drift or diffusion biased. The solution of the equations results in the potential, the charged species densities and the surface charge at each node in the mesh. The neutral species densities are updated explicitly using

$$\frac{\partial n_i}{\partial t} - \nabla \cdot D_i \nabla n_i = S_i \tag{2.4}$$

A table of transport coefficients, generated by solving Boltzmann's equation for the electron energy distribution off-line, is used to determine the electron temperature, collision frequency, and rate coefficients for electron impact reactions based on the *E/N* values calculated during the simulation. The electron transport coefficients are updated by using the momentum

transfer collision frequencies interpolated from this table. Diffusivity's and mobility's for the ions and neutral gas species do not change significantly during the simulation and are obtained via lookup tables [6].

The reaction mechanism is specified as an input to the simulator in the chemistry module along with the constants associated with the Arrhenius equation for each reaction. If the reaction is an electron impact reaction, the rate coefficient is obtained from the Boltzmann file. If the reaction does not include electrons, then the gas temperature is used to obtain the rate coefficient. The species densities are updated by semi-implicitly integrating the rate equations forward in time. Species densities on the left side of the equations are reduced while the products are increased. The plasma chemistry is coupled to the continuity equations via the source term in Equation (2.2).

Once all the densities are updated, time is incremented, the equations are re-linearized and the simulation proceeds. The time step for the simulation is based on the difficulty that the matrix solver has producing a solution to the system of equations. If the number of iterations that the solver takes significantly increases from one time step to the next, the time step for the subsequent calculation will be decreased. The time step is increased if the matrix solver produces a solution quickly. By varying the time step for the simulation, the length of the simulation can be significantly shortened.

In the following sections of this chapter a few of the algorithms mentioned above will be described in more detail. Specifically, Section 2.2 concentrates on the linearization technique used to solve the coupled set of differential equations. During this process, some geometrical terms appear that will be explained in Section 2.3. Section 2.4 describes the technique used to interpolate the *E/N* value. This is particularly important since a small change in *E/N* can result in

large fluctuations of the reaction rates. Section 2.5 elaborates on the gas chemistry used during the simulation, and Section 2.6 explains the details involved in solving the system of differential equations. Finally, Section 2.7 presents some of the limitations that must be taken into account when this model is applied to metal halide lamps.

2.2 Finite Volume Technique on Triangular Meshes

In order to solve the coupled set of equations efficiently, they must be linearized. This is straightforward on a rectilinear mesh, using finite difference techniques, but becomes more complicated when the mesh is triangular. The objective of this section is to clarify the method used to linearize the differential equations in the PSS.

The first step in this process is to associate each node with a given volume. In this region it is assumed that the potential, density, and surface charge vary linearly from node to node. This is a safe assumption in the limit that the mesh is dense enough to make the gradients across each volume small. Figure 2.2 shows a given node in the mesh and its associated volume. The nodes and the solid lines are the output from the mesh generator. By identifying the intersection of the perpendicular bisectors between a node and its nearest neighbors, a finite volume can be associated with each node. This is indicated by the area enclosed by the dotted lines and will be referred to as a cell. Since this is a two-dimensional simulation, the volume referred to is actually the area of the cell. It will be shown later that the depth term drops out of the equation and is not important.

This algorithm works fine in the bulk of the mesh, where there is a neighbor in all directions, but a special situation arises on the edge of the mesh. The problem is apparent in Figure 2.3. Each node that is on the edge of the mesh has only half the area associated with it.

To correct this problem, reflective boundary conditions are used. For every node on the boundary of the mesh, the neighbors that are not on the boundary are reflected through the boundary for the purpose of defining a cell. The node that is reflected has all the same characteristics as the original node, including potential, species densities, surface charge, and all material properties. Any fluxes going into the artificial node are added back into the original node.

The finite volumes on an actual mesh are shown in Figure 2.4. The red lines in the figure are the mesh obtained from the mesh generator. The blue lines are the volumes obtained by computing the intersection of the perpendicular bisectors as explained above. The reflective boundary conditions can also be seen at the top of the mesh.

To demonstrate how this procedure aids in solving the above equations, Equation (2.1) is discretized here. For simplicity, the term including the summation over all the charged species will be included in the ρ term. First, both sides of the equation are integrated over the cell volume.

$$\int \nabla \cdot \varepsilon \nabla \phi \, dV = -\int \rho \, dV \tag{2.5}$$

Applying the divergence theorem to Equation (2.5), the volume integral can be transformed into a surface integral.

$$\oint \varepsilon \nabla \phi \cdot dS = \rho V \tag{2.6}$$

The density term on the right-hand side of the equation is assumed to be constant over the cell volume and therefore can be pulled out of the integral. Assuming that the potential is constant across each face of the cell, the potential term, along with the epsilon, can be extracted from the integral. The integral must be performed across every face of the cell to account for all the

fluxes entering or leaving the cell. In this manner, the surface integral can be replaced with a summation over the cell perimeter:

$$\frac{1}{V}\sum_{i=1}^{neighbors}\varepsilon\nabla\phi A_i-\rho=0 \tag{2.7}$$

The gradient operator in Equation (2.7) is linearized by using a finite difference method. The convention used in this program is to define the *positive direction as pointing out of the cell*. Using this assumption, the gradient operator can be reduced to a difference between the two potentials divided by the distance between the node and its neighbor:

$$\frac{1}{V}\sum_{i=1}^{neighbors}\frac{\varepsilon(\phi_i-\phi_{node})A_i}{x_i}-\rho=0 \tag{2.8}$$

where x is the distance between the node and its neighbor. Thus the differential equations can be written as simple algebraic expressions. A similar sequence of operations is applied to the continuity equations to discretize them.

2.3 Geometry Computations

The geometry involved in solving the coupled set of differential equations on a triangular mesh is complex. The area and volume of every cell, along with the distance between every two nodes, must be calculated before the equations can be linearized. On a mesh containing several thousand nodes, these calculations can take a significant amount of time. For this reason, all geometry calculations are performed when the program starts and are stored in arrays until needed.

To compute the areas and the volumes of the cells used in (2.8), the cell corners must be identified. Referring to Figure 2.2, the cell corners are defined as the intersection of the dotted lines. The corners are found by taking the perpendicular bisectors of each line connecting a node

with its neighbor and computing where they intersect. To simplify this operation, the nodes are ordered in memory such that two adjacent neighbors are stored consecutively. As long as the intersections of these lines do not lie outside the triangle formed by the node and the two adjacent neighbors, cells will not overlap. This is important to ensure that fluxes are conserved. In this version of the simulator no additional provisions have been made in the event that two cells do overlap. To minimize the effects of round-off error associated with finite register length, tolerances have been added to all geometry calculations.

Once the cell corners are calculated, the area and volume calculations are straightforward. The area term between node *i* and neighbor *j* is simply the length of the cell face between these two nodes:

$$A_{i,j} = \sqrt{(x_{cellcorner1} - x_{ccellcorner2})^2 + (y_{cellcorner1} - y_{cellcorner2})^2} \tag{2.9}$$

The volume term is calculated based on the observation that any two adjacent cell corners form a triangle with the main node. To find the volume of the entire cell, the volume of each subtriangle is found first and then all of them are summed up:

$$V_{i,j} = \sum_{i=1}^{neighbors} \frac{a_i c_i \sqrt{1 - (\cos(\alpha_i))^2}}{2} \tag{2.10}$$

where the values *a*, *c*, and α are the lengths and the angle indicated in Figure 2.5.

Technically, Equations (2.9) and (2.10) should contain a depth term. But, because they always appear as a ratio of area divided by volume, this term cancels out. Hence, as expected, in a two-dimensional simulation, the depth of the mesh is irrelevant.

2.4 Interpolation of *E/N*

The value of *E/N* plays an important role in this simulation. The off-line Boltzmann solver generates the look-up table for electron temperature and electron impact rate coefficients based on this value. The dependence of rate coefficients on the *E/N* value is exponential. Therefore a small change in the value of *E/N* causes a large change in the rates. To emphasize how *E/N* is calculated in this model, one technique applied to rectilinear meshes will be presented here. The algorithm for the triangular mesh is very similar to rectilinear mesh with a few important differences.

The electric field calculation on a rectilinear mesh is performed by using a finite difference method. Figure 2.6 shows the arrangement of the nodes on a rectilinear mesh. The letters labeling each node will be used as subscripts to indicate direction. The electric field in each direction is calculated using:

$$E_D = -\left(\frac{\phi_D - \phi_C}{x_D} \right) \tag{2.11}$$

where ϕ_D indicates the potential at the neighbor in the direction D, either above, left, right, or below; ϕ_C is the potential at the center node; and x_D is the distance separating the node and its neighbor in each direction. The resulting electric field vectors for each direction would be located at the crosses in Figure 2.6.

Once the electric fields in each direction are calculated, the *E/N* value at the center node can be calculated by interpolating the individual vector components to obtain a vector at the center node. A vector average is then used to combine the *x* and the *y* components into a single vector using:

$$\frac{E_C}{N} = \frac{\sqrt{\left(\frac{x_L E_R + x_R E_L}{x_R + x_L}\right)_x^2 + \left(\frac{x_B E_A + x_A E_B}{x_A + x_B}\right)_y^2}}{n_{C\ total}} \tag{2.12}$$

where the x variables represent the distances between the center node and the location of the electric field vectors in each direction and $n_{c\ total}$ is the total density at the center node.

A triangular mesh poses some difficulties for the above equations. The electric field at the midpoint between a node and its neighbor can be calculated in the same manner as Equation (2.12), but this results in several vectors that point in different directions. It is difficult to interpolate the vectors surrounding the node to calculate a single electric field vector at the center node. For this reason a different interpolation scheme is used.

For a triangular mesh the potentials of the neighbors are interpolated back to the axes. The algorithm searches for the neighbors closest to both sides of every axis based on the angle of the neighbor with respect to the axes. This yields an array with eight nodes. A linear interpolation is then performed between the two nodes closest to the axis to obtain the potential value on the axis. The distance between the interpolated potential and the center node is also stored. Once the potentials are known on the axes, Equations (2.11) and (2.12) can be used to obtain the electric field at the node. All the constant interpolation factors are computed prior to the simulation to reduce computational time.

2.5 Gas Chemistry

The reaction mechanism used for this program is read in from a separate file, allowing the gas chemistry to be changed easily. The constants associated with the Arrhenius form of the rate coefficient are also supplied in this file:

$$k = A\left(\frac{T}{300}\right)^n \exp\left(-\frac{E_a}{T}\right) \tag{2.13}$$

where k is the rate coefficient, A is the frequency factor, T is the temperature, and E_a is the activation energy of the reaction. The rate for a reaction is obtained by multiplying the rate coefficient by the densities of the individual species on the left hand side of the equation:

$$r_i = k_i \prod_{j=1}^{N_S} N_{i,j}^{m_{i,j}} \alpha_{i,j} \tag{2.14}$$

where r is the rate of reaction i, k is the rate coefficient, N_S is the total number of species, $m_{i,j}$ is the stoichiometric coefficient for species j, $N_{i,j}$ are the species densities, and $\alpha_{i,j}$ is 1 for species that are on the left-hand side (LHS) of the reaction and 0 for species on the right-hand side (RHS). For reactions involving electrons, the electron densities in Equation (2.14) are factored out and are calculated implicitly in the Jacobian.

During each time step, the rates for all the reactions are calculated, as well as the change in each of the species densities. The species densities are reduced by the rate of the reaction times Δt if they are on the LHS of the reaction and are increased by the rate of the reaction if they are on the RHS. The chemistry is coupled into the differential equations via the source term in Equation (2.2).

The initial densities of all the gas species are specified as a mole fraction of the total gas density:

$$n = \alpha \frac{P}{kT} \tag{2.15}$$

where n is the total gas density, P is the total gas pressure, k is Boltzmann's constant, T is the temperature of the gas, and α is the initial percentage of the species. The initial densities are

assumed uniform over the entire plasma region. If desired, the initial electron densities can be given a Gausian profile over the plasma region thereby allowing seeding of the arc.

2.6 Solution Technique

The system of equations is solved by integrating in time. The variables for the next time step are calculated using

$$N(t+\Delta t) = N(t) + \frac{\partial N}{\partial t}\Delta t = N(t) + \Delta N \tag{2.16}$$

where N represents the potential, density, and surface charge variables at each node. Newton iterations are used to determine the ΔN values. Equations (2.1), (2.2), and (2.3) are rewritten in terms of three new functions, F_1, F_2, and F_3, respectively.

$$F_1 = \nabla\cdot(\varepsilon\nabla\phi) + \sum_{j=1}^{N_{ch}} q_j n_j + \rho \tag{2.17}$$

$$F_2 = \frac{\partial n_i}{\partial t} - \nabla\cdot(D_i\nabla n_i \pm \mu_i n_i \nabla\phi) - S_i \tag{2.18}$$

$$F_3 = \frac{\partial \rho}{\partial t} - \sum_{j=1}^{N_{ch}} q_j \nabla\cdot(D_j\nabla n_j \pm \mu_j n_j \nabla\phi) + \nabla\cdot(\sigma(-\nabla\phi)) \tag{2.19}$$

These functions are linearized using a first-order Taylor series expansion. For example, expanding Poisson's equation results in

$$\frac{\partial F_1}{\partial \phi_i}\Delta\phi_i + \frac{\partial F_1}{\partial n_i}\Delta\phi_i + \frac{\partial F_1}{\partial \rho_i}\Delta\phi_i + \cdots + \frac{\partial F_1}{\partial \phi_{i+N}}\Delta\phi_i + \frac{\partial F_1}{\partial \phi_{i+N}}\Delta\phi_i + \frac{\partial F_1}{\partial \phi_{i+N}}\Delta\phi_i = -F_1 \tag{2.20}$$

where the i is the node that is being solved for, and $i+N$ represents the dependency of the node i on all the other nodes in the mesh. Equations (2.17), (2.18), and (2.19) are all expanded and written in matrix form.

$$\begin{bmatrix} \frac{\partial F_{i,1}}{\partial \phi_i} & \frac{\partial F_{i,1}}{\partial n_i} & \frac{\partial F_{i,1}}{\partial \rho_i} & \cdots & \frac{\partial F_{i,1}}{\partial \phi_{i+N}} & \frac{\partial F_{i,1}}{\partial n_{i+N}} & \\ \frac{\partial F_{i,2}}{\partial \phi_i} & \frac{\partial F_{i,2}}{\partial n_i} & & & \frac{\partial F_{i,2}}{\partial \phi_{i+N}} & \frac{\partial F_{i,2}}{\partial n_{i+N}} & \\ \frac{\partial F_{i,3}}{\partial \phi_i} & \frac{\partial F_{i,3}}{\partial n_i} & \frac{\partial F_{i,3}}{\partial \rho_i} & & \frac{\partial F_{i,3}}{\partial \phi_{i+N}} & \frac{\partial F_{i,3}}{\partial n_{i+N}} & \\ & \vdots & & \ddots & & & \\ \frac{\partial F_{i+N,1}}{\partial \phi_i} & & & & \frac{\partial F_{i+N,1}}{\partial \phi_{i+N}} & \frac{\partial F_{i+N,1}}{\partial n_{i+N}} & \frac{\partial F_{i+N,1}}{\partial \rho_{i+N}} \\ \frac{\partial F_{i+N,2}}{\partial \phi_i} & \frac{\partial F_{i+N,2}}{\partial n_i} & & & \frac{\partial F_{i+N,2}}{\partial \phi_{i+N}} & \frac{\partial F_{i+N,2}}{\partial n_{i+N}} & \\ \frac{\partial F_{i+N,3}}{\partial \phi_i} & \frac{\partial F_{i+N,3}}{\partial n_i} & & & \frac{\partial F_{i+N,3}}{\partial \phi_{i+N}} & \frac{\partial F_{i+N,3}}{\partial n_{i+N}} & \frac{\partial F_{i+N,3}}{\partial \rho_{i+N}} \end{bmatrix} \begin{bmatrix} \Delta\phi_{i,g} \\ \Delta n_{i,g} \\ \Delta\rho_{i,g} \\ \vdots \\ \Delta\phi_{i+N,g} \\ \Delta n_{i+N,g} \\ \Delta\rho_{i+N,g} \end{bmatrix} = \begin{bmatrix} -F_{i,1} \\ -F_{i,2} \\ -F_{i,3} \\ \vdots \\ -F_{i+N,1} \\ -F_{i+N,2} \\ -F_{i+N,3} \end{bmatrix} \tag{2.21}$$

An initial guess for Δn is calculated using a linear interpolation from the previous time step:

$$\Delta n_g = \frac{\Delta t_1}{\Delta t_2}\left(N_1 - N_2\right) \tag{2.22}$$

where Δn_g is the initial guess for Δn, Δt_1 and Δt_2 are the two previous time steps, and N_1 and N_2 are the variables from the previous two time steps. The matrix is solved for new Δn values, and the solution is checked against a specified error criteria. If the solution does not meet the convergence criteria, then the guess is refined.

$$\Delta n_{g\,next} = n_g + \Delta n_g \tag{2.23}$$

The Jacobian matrix and the matrix on the RHS of Equation (2.21) are updated using the new guess, and the equations are solved again. This process is repeated until the error criterion is satisfied. At this point, the Δn values in Equation (2.21) are substituted for ΔN values in Equation (2.16) to obtain $N(t+\Delta t)$.

The matrix solver used to solve the set of equations was obtained from the SLAP Sparse Matrix Library from Oak Ridge National Laboratory [7] and Seager [8]. The matrix solver uses

a biconjugate gradient spare matrix solution technique with incomplete LU factorization for preconditioning.

2.7 Limitations of the Model

There are several limiting factors when it comes to simulating metal halide lamps. For example, the lack of thermal equations and complete reaction mechanisms limit this program from fully simulating commercial metal halide lamps.

As mentioned in Chapter 1, the high temperatures in metal halide lamps play a large role in gas chemistry, sputtering processes, and CRIs. Without support for thermionic emission from the electrodes, the steady-state development of the arc cannot be studied completely. For this reason, this thesis is limited to simulating the breakdown phase of lamps. In this region it is safe to assume that the lamp is in thermal equilibrium with its environment.

The second limitation arises from the complex gas chemistry in metal halide lamps. In order to fully capture this chemistry, the rate coefficients for all possible reactions must be known. Because most lamps include doses of several different metals, this is extremely difficult, if not impossible. To complicate the matter further, the metals exist in several states of matter at different locations due to the large thermal gradients between the arc and the quartz wall. The final concern is the computational time necessary to solve such a system of equations. The maximum time step is limited by the smallest reaction rate. If this limit is exceeded, then the gas chemistry could cause the solution of the equations to diverge. The parameterization performed in the next chapter uses pure argon.

The model presented in this chapter is sufficient to represent the trends involved in the design of metal halide lamps, but is not sufficiently complex to capture all of their properties.

Chapter 4 of this thesis presents some of the future work that can be performed to close the gap between reality and simulation.

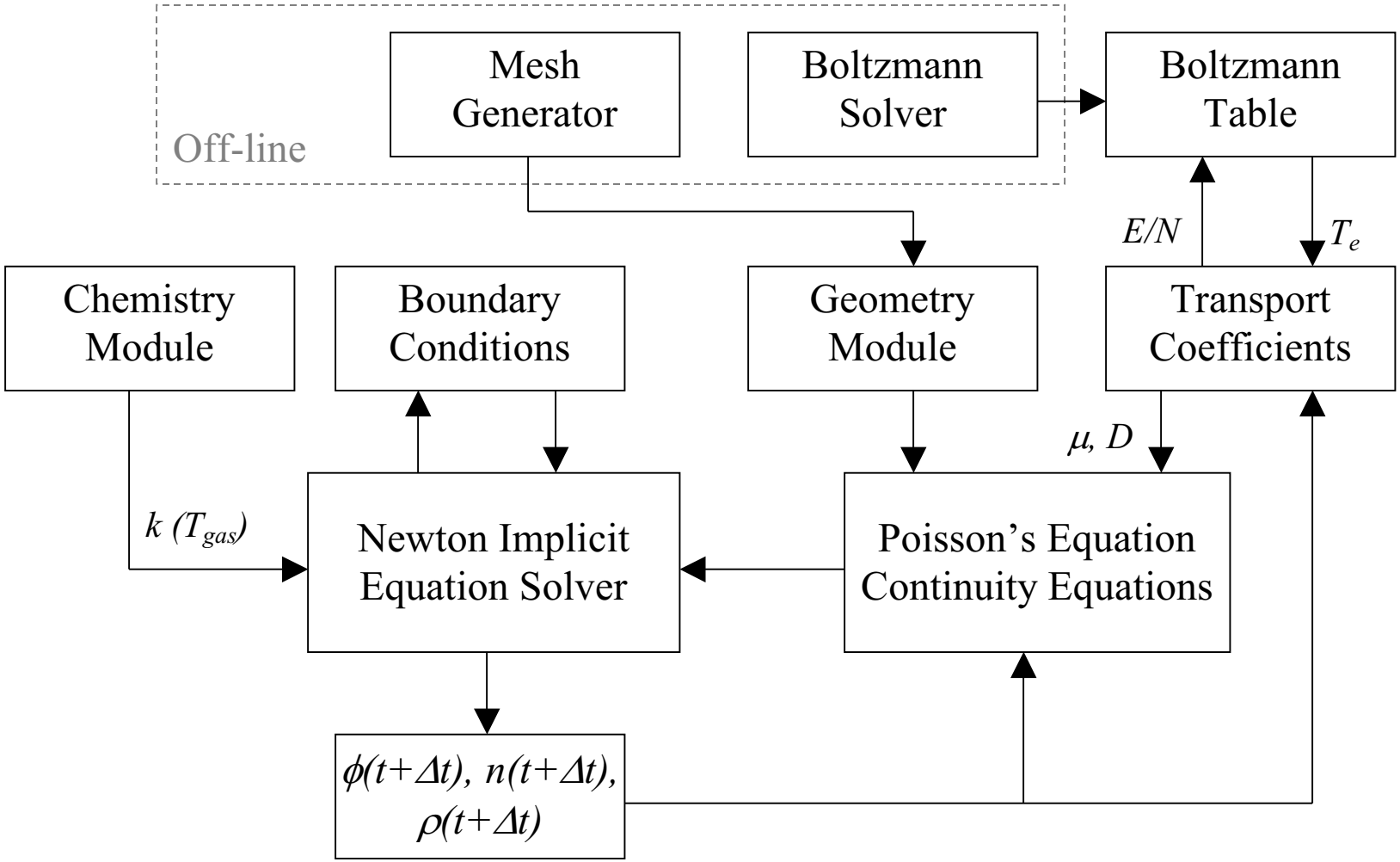

Figure 2.1 Block diagram of the Plasma Solid Simulator (PSS).

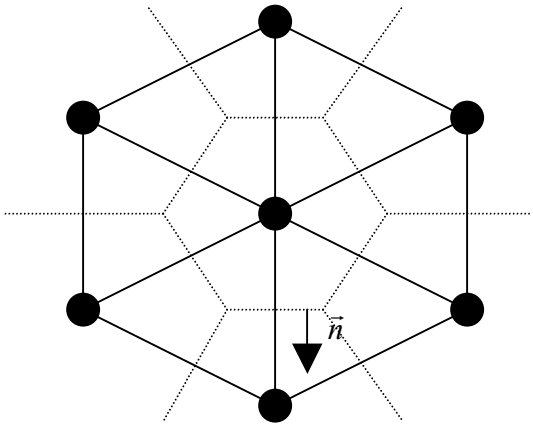

Figure 2.2 Typical triangular mesh. Solid lines are the mesh, and the dotted lines indicate how the mesh is discretized into cells.

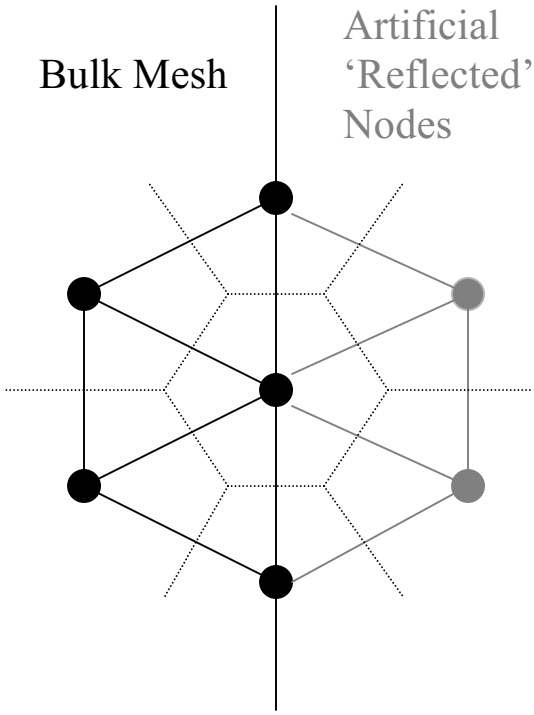

Figure 2.3 Reflective boundary conditions on the edge of the mesh. Artificial nodes are inserted so that a complete cell is formed. All the properties of the original node are copied to the reflected node.

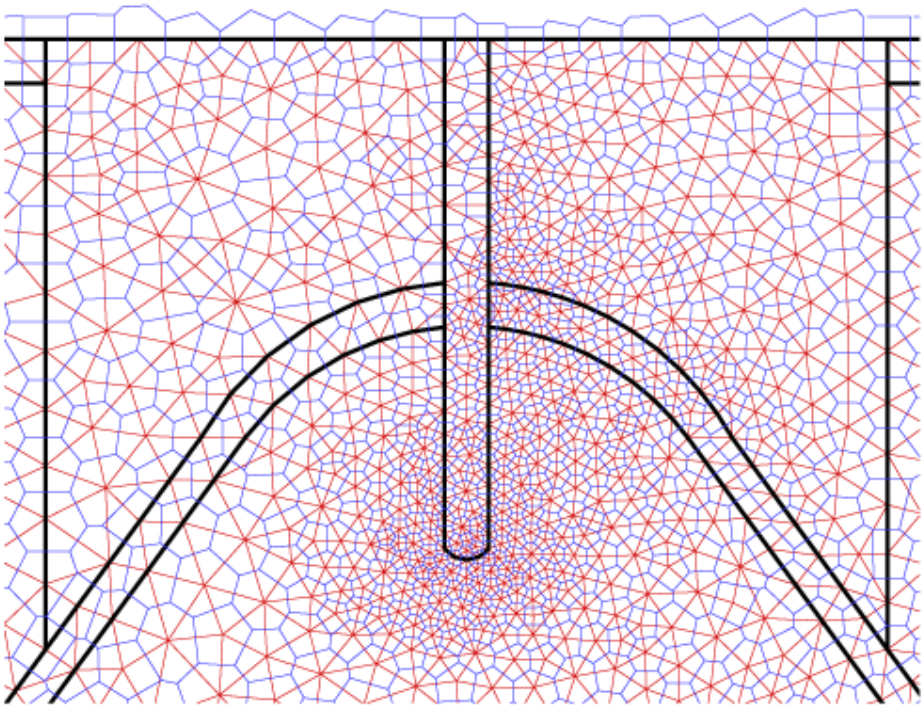

Figure 2.4 Finite volumes on an actual mesh. The red lines indicate the mesh and the blue lines indicate the perimeter of the finite volumes associated with each mesh point.

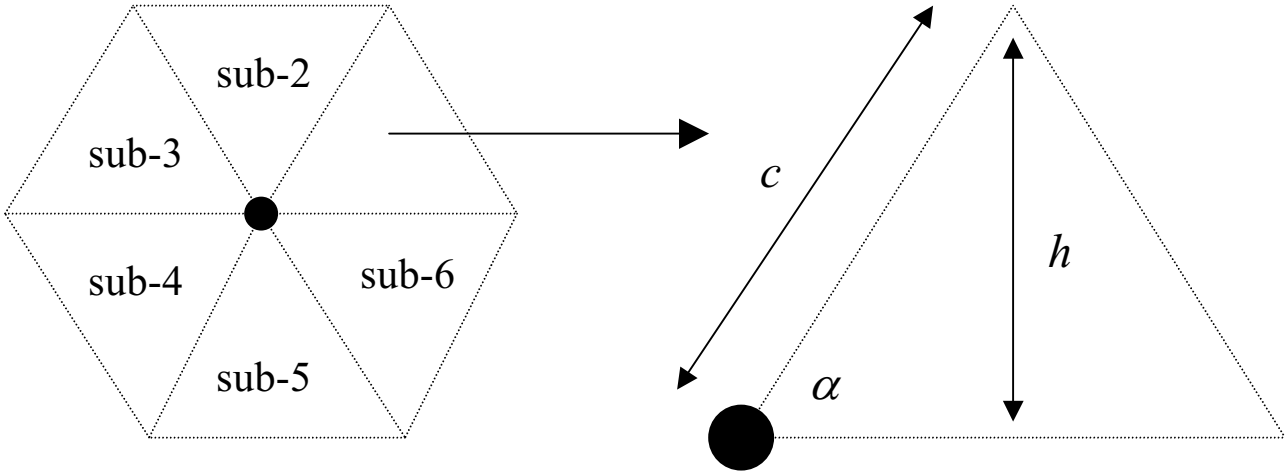

Figure 2.5 Calculation of the cell volume. Each region is calculated separately, and then all the volumes are summed to obtain the total volume.

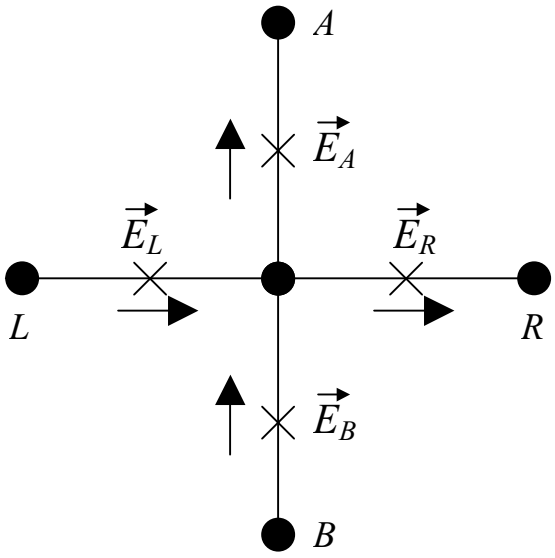

Figure 2.6 Calculation of *E/N*. A finite difference technique is used to compute the electric field at the midpoint between two nodes. A vector average is used to obtain the *E/N* value at the center node.

2.8 References

[1] S. Rauf and M. Kushner, J. Appl. Phys., **85**, 3460 (1999).

[2] L. C. Pitchford, I. Peres, K. B. Liland, J. P. Boeuf, and H. Gielen, J. Appl. Phys., **82** (1), 112 (1997).

[3] I. Peres and L. C. Pitchford, J. Appl. Phys., **78** (2), 774 (1995).

[4] D. L. Scharfetter and H. K. Gummel, IEEE Trans. Electron Devices, **ED-16**, 64 (1969).

[5] K. Kramer and N. Hitchon, *Semiconductor Devices: A Simulation Approach* (Prentice Hall, Upper Saddle River, NJ, 1997) p. 227.

[6] J. O. Hirschfelder, C. F. Curtiss, and R.B. Bird, *Molecular Theory of Gases and Liquids* (Wiley, New York, NY, 1954) p. 539.

[7] SLAP Sparse Matrix Library, http://www.netlib.org.

[8] M. K. Seager, Lawrence Livermore National Laboratory Technical Report UCRL-100195 (1988), http://www.llnl.gov.

3. SIMULATION OF METAL HALIDE LAMPS

3.1 Introduction

In this chapter, results of the simulations performed on metal halide lamps are discussed. Parameterizations were performed for several voltages, secondary electron emission coefficients, and pressures. A full parameterization of the starting process using an ignition probe is also presented.

Section 3.2 describes the lamp geometry used throughout the simulations. Section 3.3 describes the base case. Section 3.4 reports the results of the parameterizations for voltages, secondary electron coefficients, and pressures. Finally, Section 3.5 investigates how the lamp parameters are affected by applying a voltage to the starter probe.

3.2 Lamp Geometry

The lamp geometry used for these simulations is shown in Figure 3.1. The lamp consists of a cathode and an anode opposing each other with a gap distance of 4.7 cm. The cathode and anode enter the quartz tube through two pieces of ceramic modeled as simple dielectrics. The arc forms within a quartz cylinder that has a diameter of 3 cm. The quartz cylinder is surrounded by air and the lamp is placed within a ground plane. The ground plane was included in the simulation to provide boundary conditions for the solution of Poisson's equation. A starter probe, positioned near the cathode, is also included in the simulation. This provides a simple method to obtain a second source of ionizations inside the arc tube without altering the model.

The mesh used during these simulations is also shown in Figure 3.1. The mesh was graded such that the points converged near the tips of the electrodes where electric field

enhancement occurs. In the bulk plasma, where electric fields are smaller, the density of nodes was decreased to save computational time. Several hundred points were placed between the starter probe and the cathode to resolve the plasma in this region. The unstructured mesh also allows curved surfaces to be modeled accurately. Although the solution of the equations should be completely independent of the mesh, in reality, this is not possible. For this reason, the mesh was not changed throughout the parameterizations.

3.3 Base Case

The base case chosen for this simulation consists of the following parameters. The relative permittivities of the dielectric, plasma, quartz, and air were 2.0, 1.0, 4.0, and 1.0, respectively. The electrodes were modeled having a secondary electron emission coefficient of 1.0 to reflect the low work function materials typically used. The pressure in the lamp was maintained at 100 Torr, and the gas temperature was held constant at 300 K. The gas chemistry consisted of a 100% argon mixture whose reaction mechanism can be found in Table 3.1. Surface charge was allowed to accumulate on the quartz wall.

The voltage pulse, shown in Figure 3.2, was applied to the anode of a lamp with an initial ionized mole fraction of $\angle\ 1.0\times10^{-10}$. The initial electron temperature was assumed to be 2.5 eV. Because a typical lamp is operated at 60 Hz, and the simulations performed on these lamps were on the order of thousands of nanoseconds, the discharge was assumed to be DC. The voltage had a finite rise time and was sustained throughout the simulation.

The results of the simulation after 15 ns are shown in Figure 3.3. This is a snapshot of the lamp parameters after the pulse had reached its maximum value. The potential contours in Figure 3.3(a) are concentrated around the tip of the anode. The large potential drop causes large

electric fields to form in this region, as shown in Figure 3.3(b). Because the power deposition in the plasma is proportional to the electric field squared, the majority of the power is deposited near the tip of the anode. This heats the electrons locally, and as a result, the electron temperature increases as shown in Figure 3.3(c). The increase in the electron temperature elevates ionization rates, and thus, the electron density increases in this region, as shown in Figure 3.3(d).

As the simulation progresses, the high concentration of electrons in front of the anode causes the plasma to become more conductive. This gradually shifts the potential contours towards the center of the lamp. The potential is shown in Figure 3.4(a), 240 ns into the simulation when the lamp has reached breakdown. Breakdown, for the purpose of this thesis, is defined quantitatively as when the electron density in the center of the lamp reaches 1.0×10^{17} m^{-3}. The electric fields, shown in Figure 3.4(b), are large near the anode and the starter probe due to electric field enhancement, but are uniform near the anode where the large electron densities are present. The electron temperature, shown in Figure 3.4(c), mimics the electric field. The electron temperature is related to the electric fields through the Boltzmann equation. The electron density, shown in Figure 3.4(d), emphasizes two very important points. First, the source terms for the electrons are located at the tip of the electrodes. This is a reasonable result since the electric fields are large in this region. Second, the transport of the electrons plays an important role in the formation of the arc. From this figure it is apparent that the electrons migrate from the electrodes to the bulk plasma to form the arc.

Once a conductive path between the two electrodes forms, the lamp impedance begins to drop and the current through the plasma increases rapidly. In a real lamp the ballast would adjust

for this changing impedance by limiting the current. In the absence of an external circuit model, a reasonable means to simulate this is to decrease the voltage across the lamp.

The fully developed arc is shown in Figure 3.5. After 400 ns, the potential drop across the bulk plasma, shown in Figure 3.5(a), is relatively small. This is an indication that the electron density in the plasma is large enough that the plasma is conductive. The electric fields, shown in Figure 3.5(b), indicate little variation down the vertical axis of the lamp but show fringing field effects towards the walls. The electron temperature contours in Figure 3.5(c) take on the same appearance as the *E/N*. The electron density shown in Figure 3.5(d), displays a fully developed arc when the electron density in the center of the lamp has reached 6.0×10^{17} m^{-3}. Without the ability to model thermionic emission from the electrodes, the simulation results beyond this point are not representative of an actual lamp.

The effect of several parameters on the base case is analyzed in the next section. By comparing the results of the parameterization to the base case presented above, one can investigate the trends that occur in actual metal halide lamps.

3.4 The Effect of Changing Parameters on the Base Case

An investigation was conducted to determine the influence of several operating parameters on the base case. The variables chosen for this study include the applied voltage to the lamp, the secondary electron emission coefficient for the electrodes and the gas pressure in the lamp. For each of these variables, the time required for the lamp to break down and the peak electron density after 400 ns were noted.

The voltage applied across the lamp has a large effect on the time required for the lamp to break down. The time until breakdown exponentially decreases as the voltage is increased, as

shown in Figure 3.6. The time until breakdown is determined solely on the electron density in the center of the lamp. The exponential relationship can be attributed to the exponential increase in the electron impact rate coefficients as a function of *E/N*. As the applied voltage is increased, the electric fields increase linearly, as does the electron temperature; however, the rate coefficients in the plasma increase exponentially.

The peak electron density after 400 ns as a function of the applied voltage is shown in Figure 3.7. As the applied voltage increases, the peak electron density also increases. Increasing the voltage elevates the electron impact rate coefficients, causing ionizations to occur faster and more electrons to be produced. Because electron production is larger, the electron density at a fixed time is expected to be greater with a higher voltage.

The dependency of the lamp breakdown on the secondary electron emission coefficients of the electrodes is shown in Figure 3.8. We found little variation in breakdown time over the range of secondary electron emission coefficients examined. This result was a little unexpected because the density in front of the electrode tip is so large, making the secondary electron source term large. Two possible reasons can explain this result. First, the voltage may be so large such that the ionization sources dominate over the secondary electron emission source terms. If the electric fields in the plasma are high enough such that ionizations occur in the bulk plasma, then the secondary electrons should have little effect on the breakdown of the lamp. Second, because the time scales are so short in these simulations, the electrons that are generated via this mechanism do not have enough time to diffuse to the center of the lamp.

The final parameter evaluated was the pressure in the lamp. The effect of varying the pressure on the breakdown time of the lamp is shown in Figure 3.9. As the pressure in the lamp increases, the arc takes a longer time to form. As pressure increases, the background argon

density also increases. This in turn decreases the *E/N* values in the lamp, thereby lowering the rate coefficients for the ionization reactions. Because the production rate for electrons is lower in the high-pressure lamp, the lamp should require a longer time to break down. Typically the applied voltage is scaled with the pressure to maintain a constant E/N.

The electron density as a function of pressure is shown in Figure 3.10. As the pressure in the lamp increases, the electron density after 400 ns decreases. This is a clearer way to demonstrate the effect of pressure on reaction rates. Because the electron density is a direct reflection of the production rate of electrons, a decrease in the electron density implies that the rate of electron production decreases as long as the loss terms have remained constant. It is expected that, in higher-pressure lamps, it should take longer to achieve the same electron density because electron production is slowed.

3.5 Effect of the Starter on Lamp Operation

This section presents a parameterization of the plasma that forms as a result of pulsing the starter probe. The starter probe assists in pre-ionizing the gas so that sputtering is minimized during the ignition process. The goal of this section is to understand how the starter probe affects the ignition process.

The starter probe was initially analyzed separately in order to understand its operation. The waveform shown in Figure 3.11 was applied to the starter probe in order to create plasma between the starter probe and the electrode. Several of the plasma parameters are shown in Figure 3.12 immediately after the voltage pulse reaches its maximum value. The potential contours in Figure 3.12(a) indicate that there are large gradients between the starter probe and the cathode of the lamp. The large potential gradients result in large electric fields in this region, as

shown in Figure 3.12(b). This in turn elevates the rate coefficients and locally increases the plasma density in this region. As a result, the collision frequency increases, as shown in Figure 3.12(c). The power deposited into the plasma also heats the electrons, and the electron temperature increases as shown in Figure 3.12(d).

In order for the plasma formed between the starter probe to have any effect on the ignition of the lamp, it must diffuse to the region where the arc forms. To allow the diffusion to occur, the pulse was turned off, and the electron density was observed. The result of this simulation is shown in Figure 3.13. Figure 3.13(a) shows the density shortly after the starter probe is turned off. The plasma density is large between the two electrodes and is concentrated in a small region where the highest electric fields occur. As time progresses, the plasma density begins to decrease as a result of recombination on the electrode surfaces. In Figure 3.13(b), after 1500 ns, the peak plasma density decreases, and the plasma begins to diffuse to areas of lower densities. The location and density of the plasma after 10 000 ns has elapsed is shown in Figure 3.13(c). Finally, the plasma density after 22 000 ns is shown in Figure 3.13(d).

There are two important points to observe from this sequence. First, the plasma density in front of the cathode starts to increase. If the simulation were continued for a longer duration, the plasma would continue to diffuse towards the center of the arc tube and increase the density at the tip of the cathode. Second, it is noticed that the plasma is beginning to split in two, with a lower half and an upper half. The peak electron density is located in the upper half of the plasma, and the lower half of the plasma appears to be dying away. This reinforces the fact that the electrodes are losses for the plasma. The lower half of the plasma is surrounded on two sides by electrodes. Electrons are lost to the electrodes, and thus, the plasma begins to decay in this region. On the other hand, the upper half of the plasma only borders the cathode, and the loss

term is smaller. For this reason the peak plasma density begins to diffuse towards the tip of the cathode.

The simulation shown in Figure 3.13 took approximately 24 hours to complete on a Compaq Alpha 667-MHz processor. That implies a complete simulation from start to finish, with the starter probe to pre-ionize the gas, time to allow the plasma to diffuse, and then the voltage across the entire lamp, the simulation time per case is quite long. To reduce this time, the plasma density in the vicinity of the cathode was simply initialized to a Gausian profile as shown in Figure 3.14.

The final simulations performed using the starter probe were intended to ascertain the effect that the initial plasma density has on the breakdown of the gas. Several voltages were applied across the entire lamp using the initial conditions described above. The time until the lamp broke down was measured for each of the cases and compared against the base case. The time differences between breakdown for the nominal case and the case with the "starter" initial conditions are shown in Figure 3.15. As the potential across the lamp increases, the time difference decreases. At higher voltages the breakdown occurs in a shorter amount of time and so it is expected that the time difference is smaller. The fractional decrease in breakdown time is shown in Figure 3.16. As the voltage decreases, the starter initial conditions have a smaller fractional effect on the breakdown of the lamp. This is not the result that was expected. It was expected that at lower voltages the starter initial conditions would have a larger fractional effect on the breakdown of the gas to coincide with the larger absolute effect.

Two theories may explain this discrepancy. First, the lamps that have lower voltage applied to them take longer to break down. The diffusion process is slow in high-pressure lamps, but Figure 3.13 also shows that the peak plasma density decreases rapidly due to recombination

on the electrodes. Thus, by the time the electric fields in the lamp with a low applied voltage begin to accelerate the breakdown of the lamp, the initial plasma density placed in front of the cathode has already begun to decay. In the case when a higher applied voltage, the electric fields necessary to breakdown the lamp are achieved rapidly and the initial electrons placed in front of the cathode play a greater role in the breakdown process.

Second, these results could also imply that there are other processes occurring in the metal halide lamp that are not captured by the model. One process that may be important during the ignition process is photoionization. The initial plasma density formed by the starter probe is confined to the bottom of the lamp. It takes a long time for the diffusion process to increase the electron density in front of the cathode, or for that matter in the center of the arc tube. In reality, the photons emitted by the exited metals in this initial plasma rapidly travel to the center of the arc tube and have the potential to ionize the gas in the center of the arc tube. This transport mechanism, not included in this model, can also play an important role in the breakdown of the metal halide lamp.

The simulations performed using the starter probe demonstrate several important processes that contribute to the breakdown of the lamp. By far the most important is the transport mechanisms involved in the early stages of the lamp breakdown.

Table 3.1 Reaction mechanism and rate coefficients used for the simulations.

Reaction	**Rate Coefficient[(a)]**
$e + Ar \rightarrow Ar^* + e$	(b)
$e + Ar \rightarrow Ar^+ + e + e$	(b)
$e + Ar^* \rightarrow Ar^+ + e + e$	(b)
$e + Ar_2^* \rightarrow Ar_2^+ + e + e$	$1.8\times10^{-7}\ (T_e/300)^{0.67}\ \exp(-3.66/T_e)$
$e + Ar^* \rightarrow Ar + e$	(b)
$e + Ar_2^+ \rightarrow Ar^* + Ar$	$6.0\times10^{-7}\ (T_e/300)^{-0.67}$
$Ar^* + Ar^* \rightarrow Ar^+ + Ar + e$	5.0×10^{-10}
$Ar^+ + Ar \rightarrow Ar + Ar^+$	4.6×10^{-10}
$Ar^* + Ar + Ar \rightarrow Ar_2^* + Ar$	$1.14\times10^{-32}\ cm^6s^{-1}$
$Ar^+ + Ar + Ar \rightarrow Ar_2^+ + Ar$	$2.5\times10^{-31}\ cm^6s^{-1}$
$Ar_2^* \rightarrow Ar + Ar$	$6.0\times10^{7}\ s^{-1}$
$Ar^* \rightarrow Ar$	$1.0\times10^{7}\ s^{-1}$

(a) - The units are cm^3s^{-1} unless otherwise noted.
(b) - These rate coefficients are obtained by integrating the cross section with the electron energy distribution function which varies with position and time.

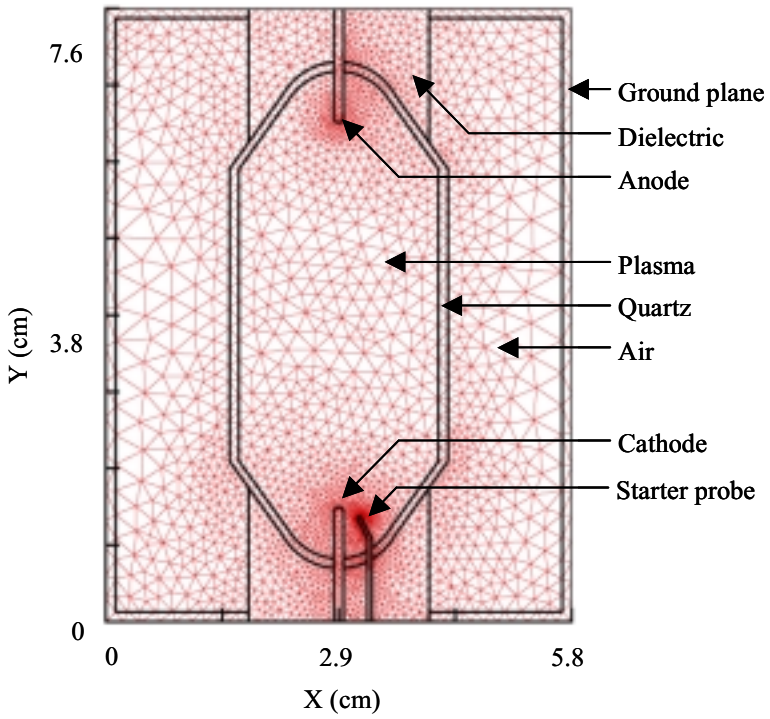

Figure 3.1 Lamp geometry and mesh. This is unchanged throughout all the simulations.

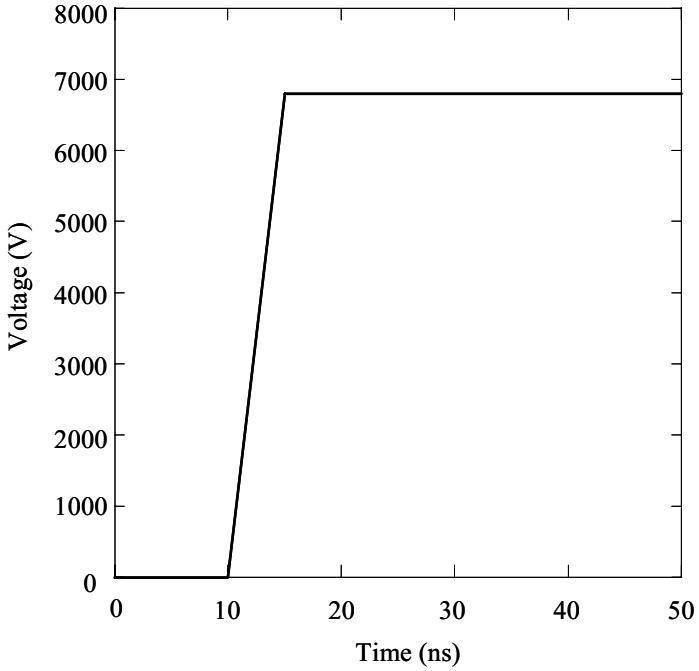

Figure 3.2 Voltage pulse applied to lamp.

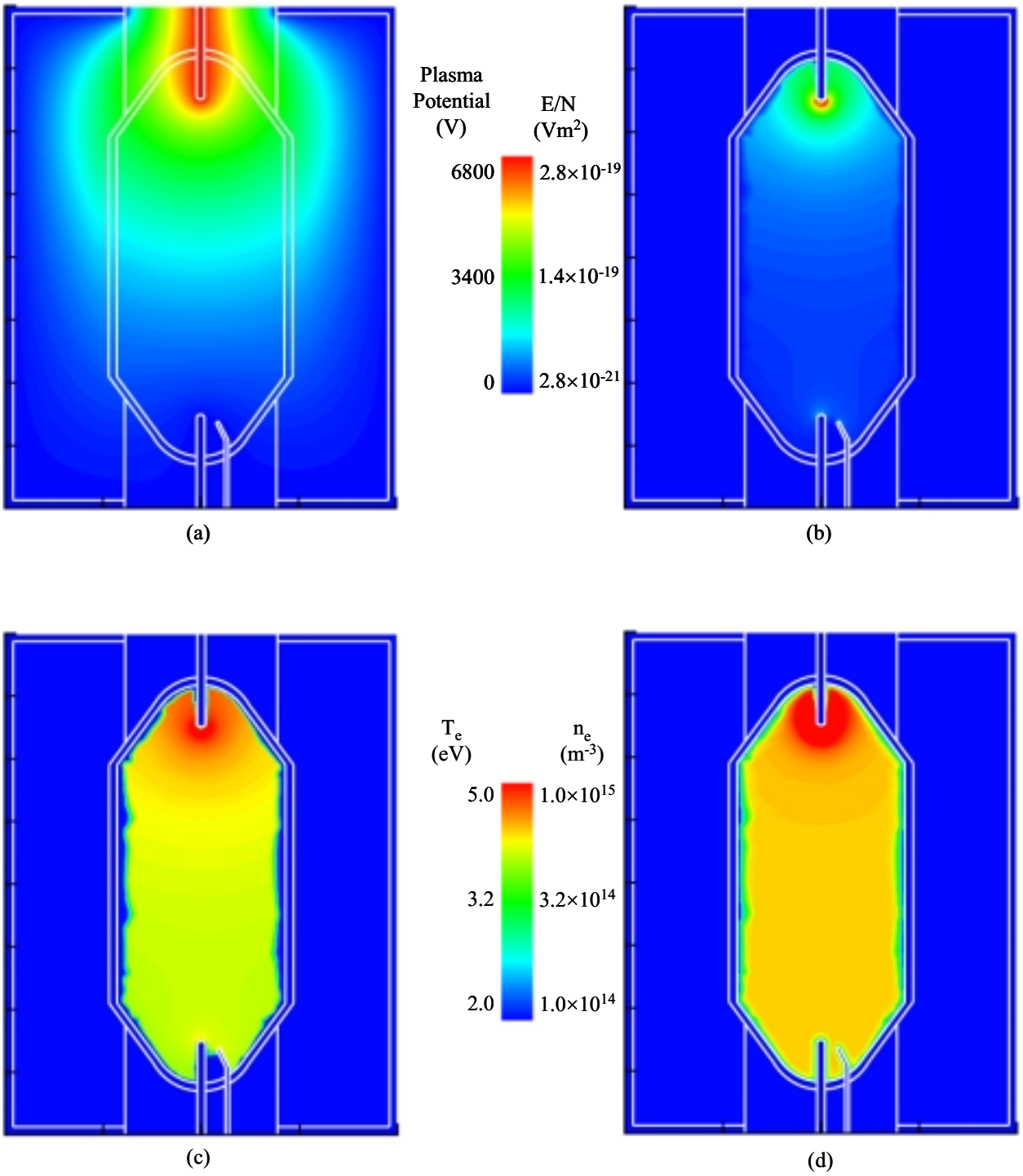

Figure 3.3 Lamp parameters immediately after the voltage reaches its maximum value at 15 ns. (a) Electric potential, (b) *E/N*, (c) electron temperature, and (d) electron density.

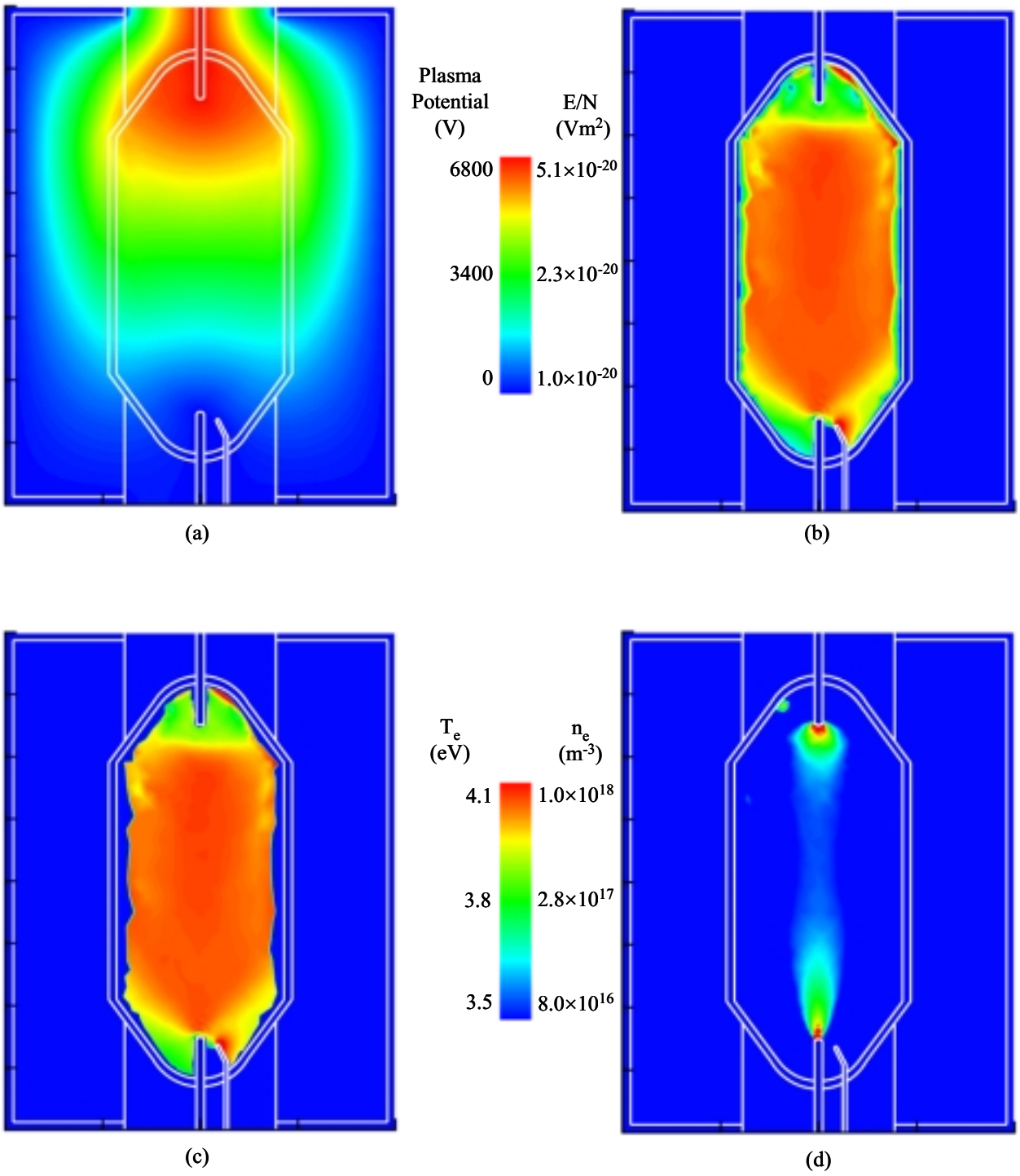

Figure 3.4 Lamp parameters immediately after breakdown at 240 ns. (a) Electric potential, (b) *E/N*, (c) electron temperature, and (d) electron density.

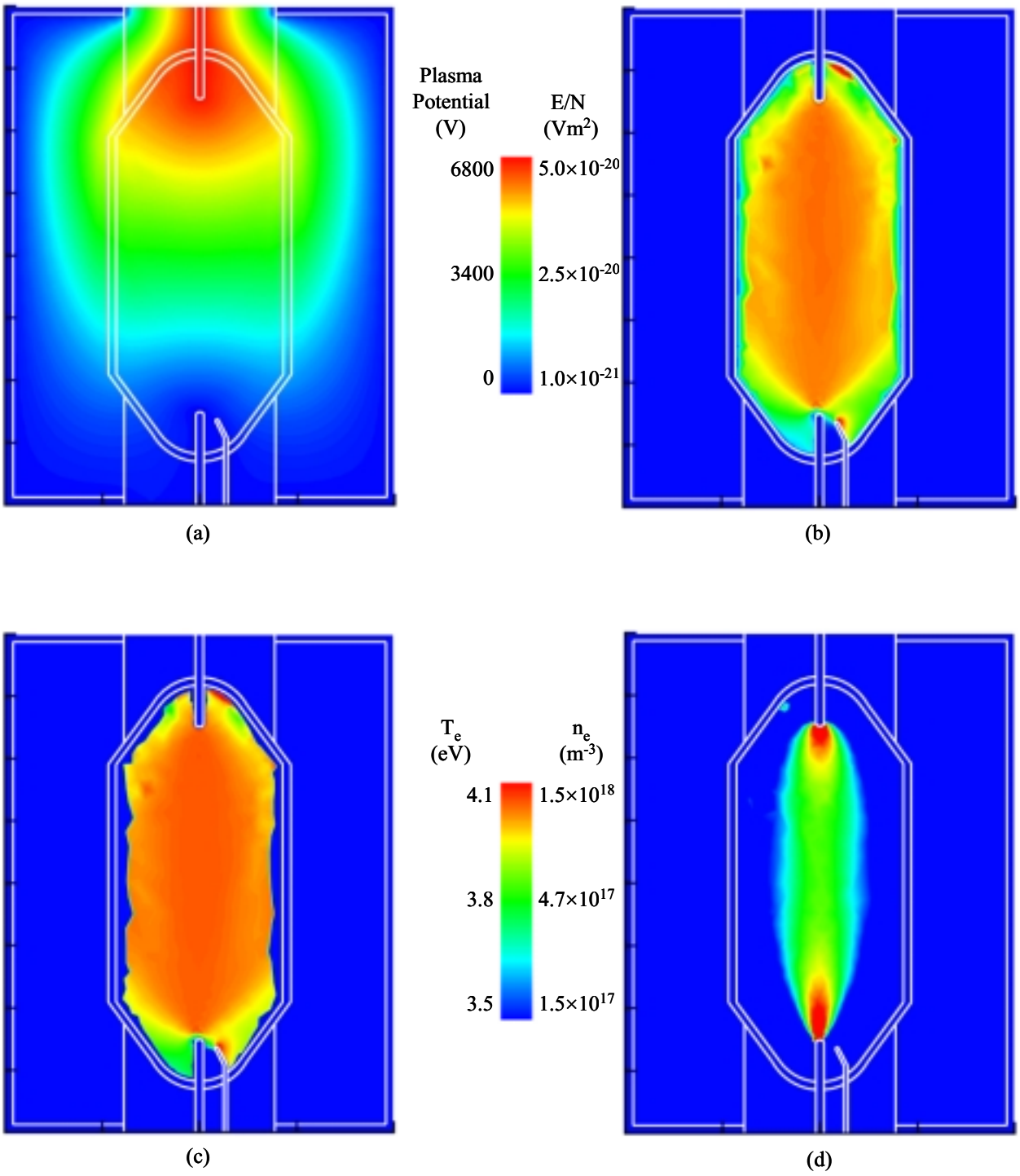

Figure 3.5 Lamp parameters after the arc has developed at 400 ns. (a) Electric potential, (b) *E/N*, (c) electron temperature, and (d) electron density.

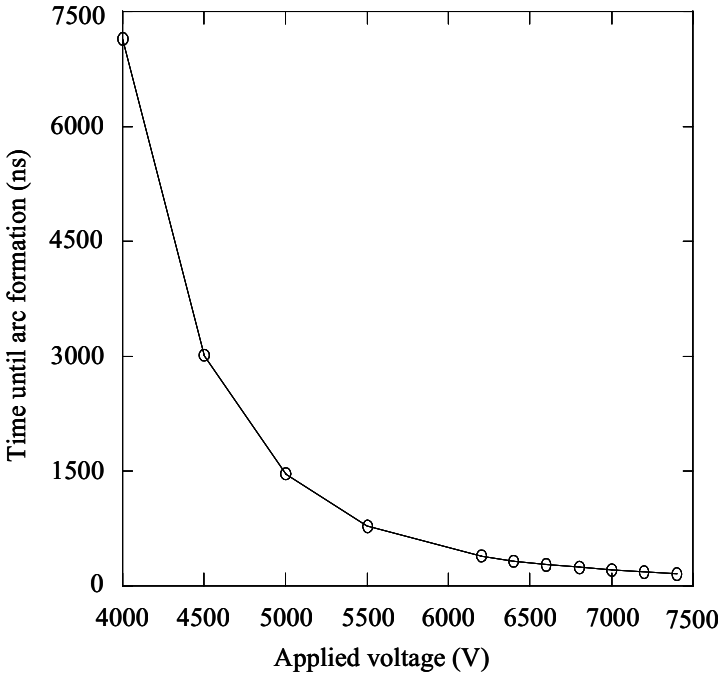

Figure 3.6 Time until breakdown as a function of applied voltage to the lamp.

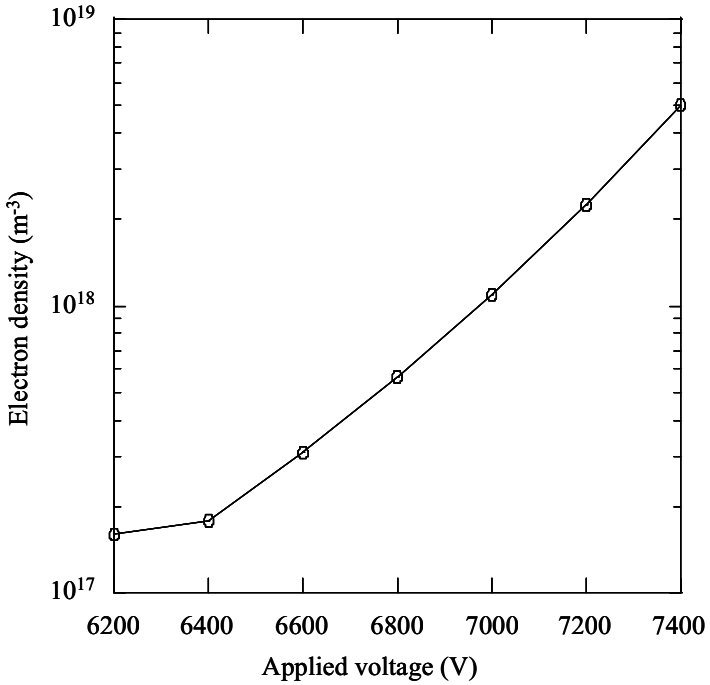

Figure 3.7 Electron density as a function of applied voltage to the lamp after 400 ns.

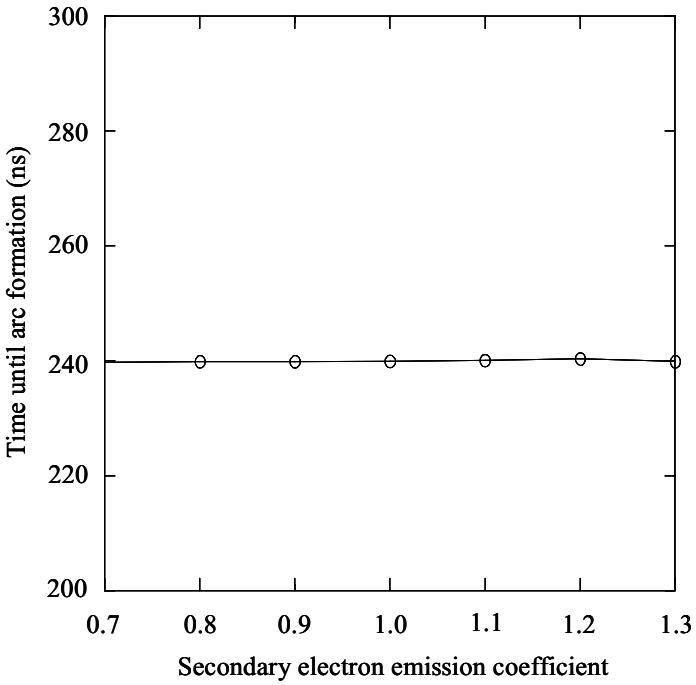

Figure 3.8 Time until breakdown as a function of the secondary electron emission coefficient.

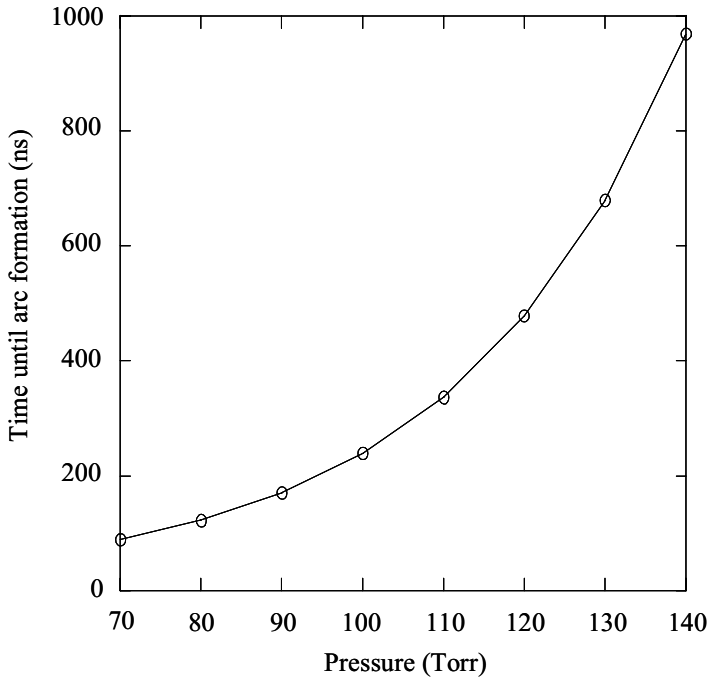

Figure 3.9 Time until breakdown as a function of the secondary electron emission coefficient.

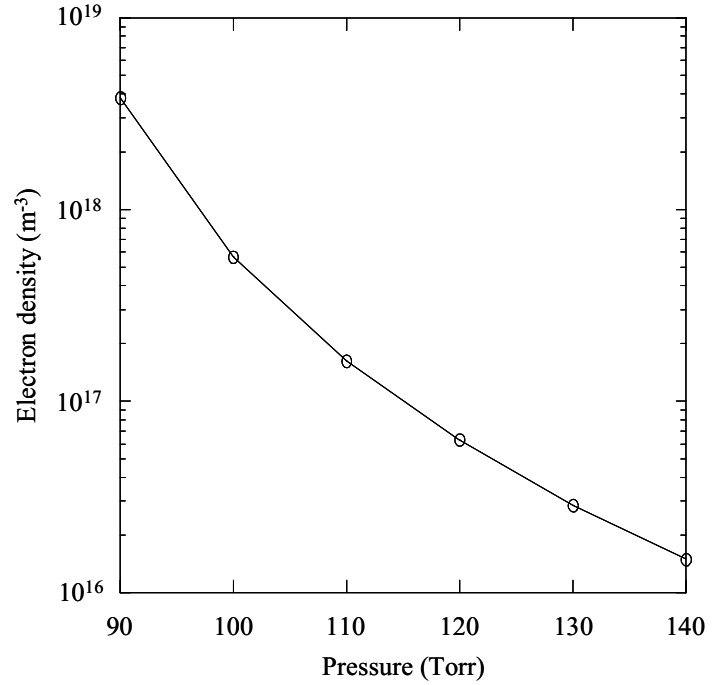

Figure 3.10 Time until breakdown as a function of the secondary electron emission coefficient.

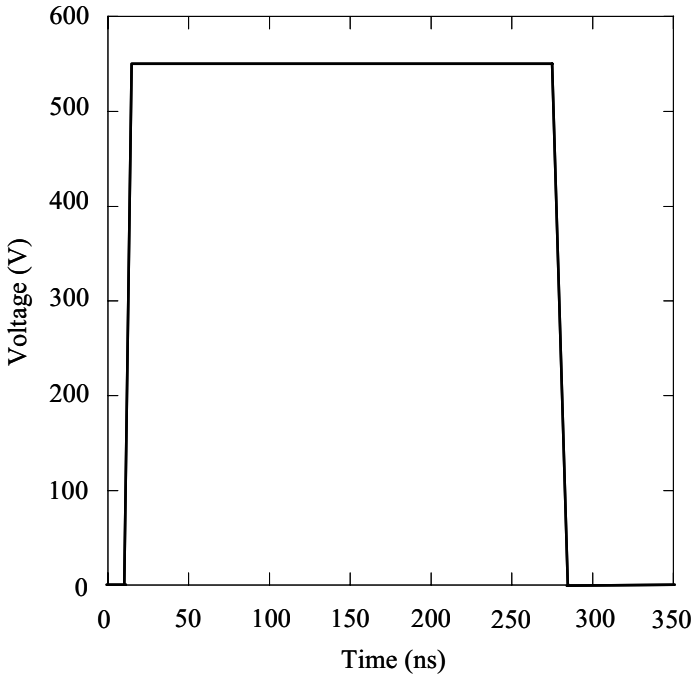

Figure 3.11 Voltage pulse applied to the starter probe.

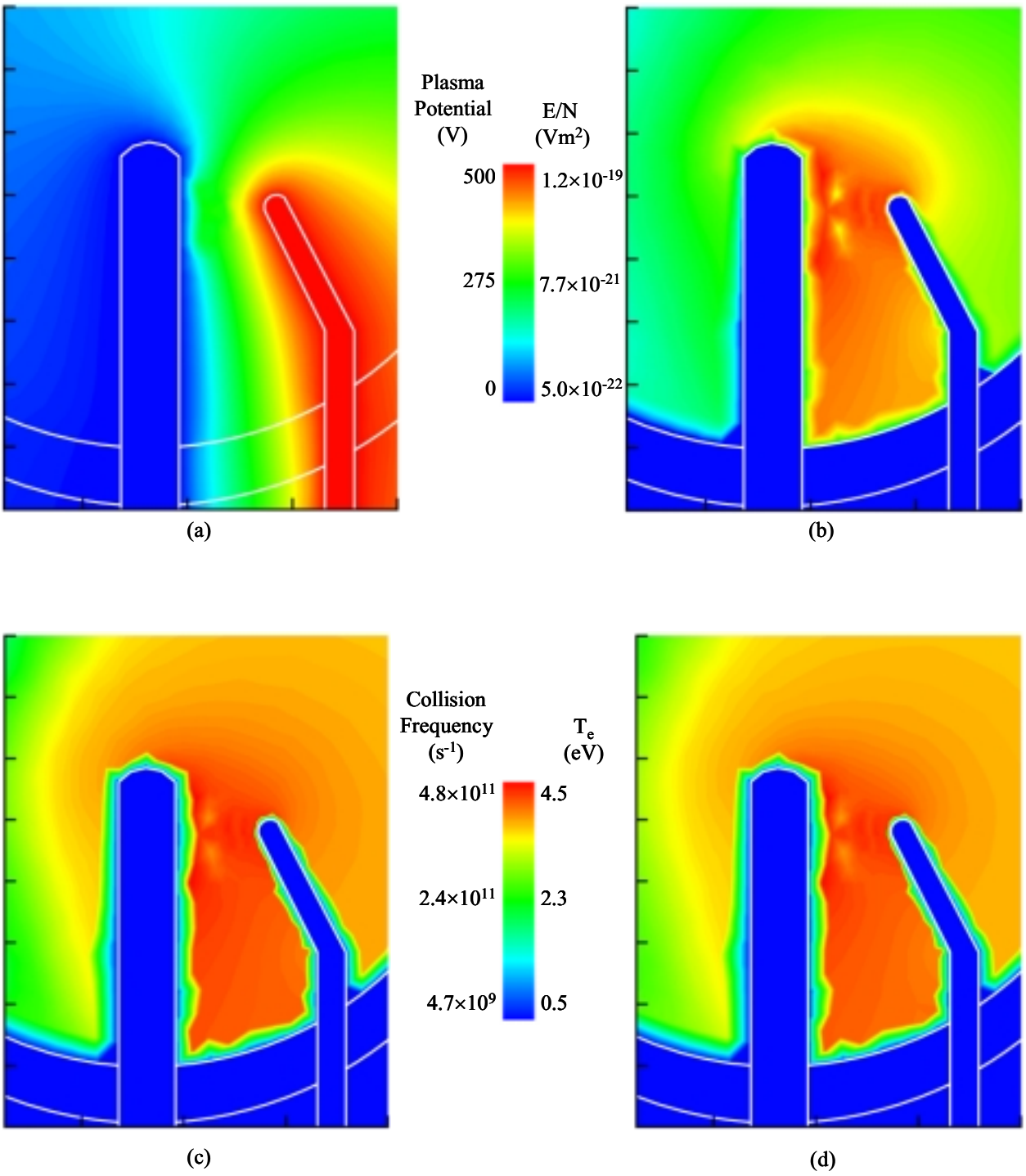

Figure 3.12 The effects of pulsing the starter on the plasma. (a) Electric potential, (b) electric fields, (c) collision frequency, and (d) electron temperature

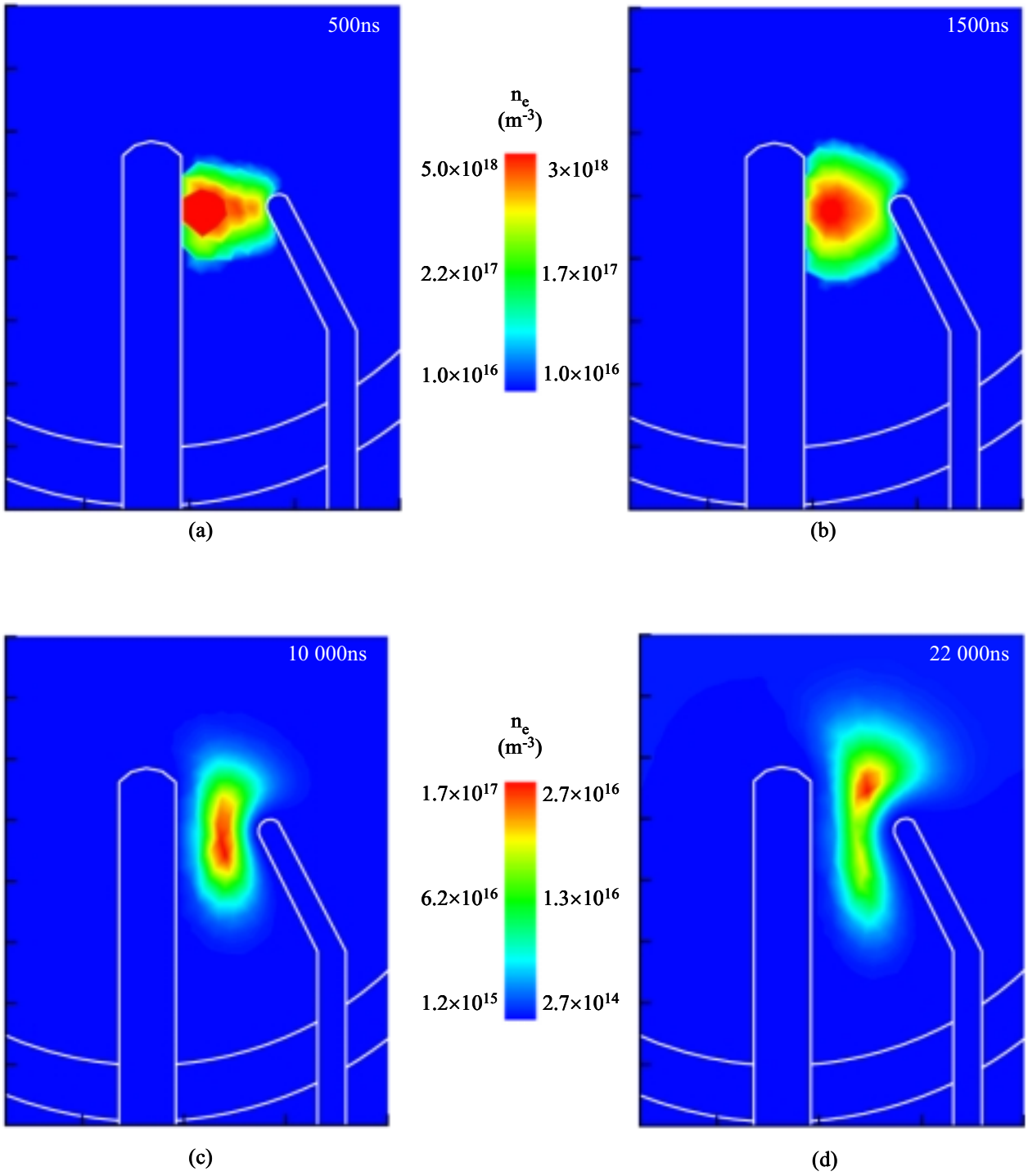

Figure 3.13 Electron density as a result of pulsing the starter. (a) Shortly after the pulse has turned off at 500 ns, (b) 1500 ns, (c) 10 000 ns, and (d) 22 000 ns.

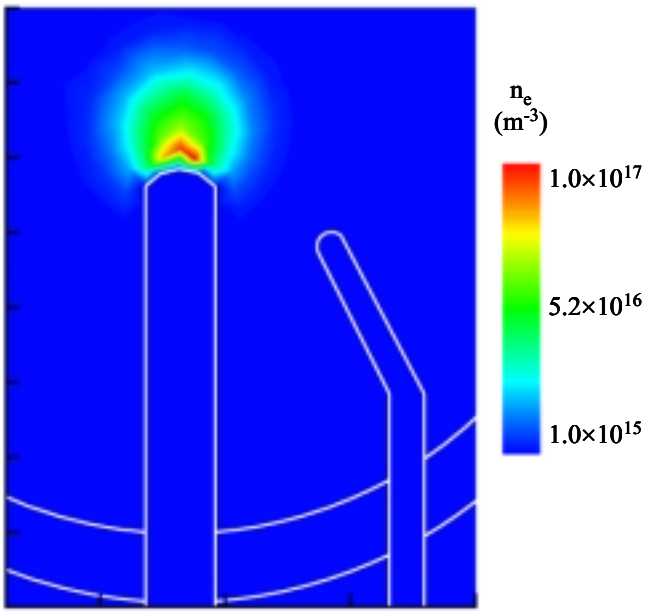

Figure 3.14 Initial conditions for the electron density used to save computational time.

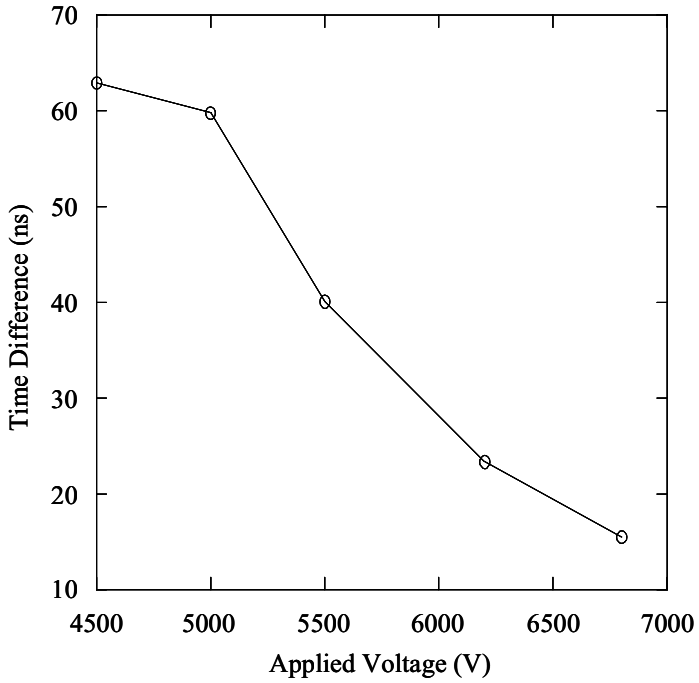

Figure 3.15 Time difference between breakdown of the cases using the "starter" initial electron density and the nominal case.

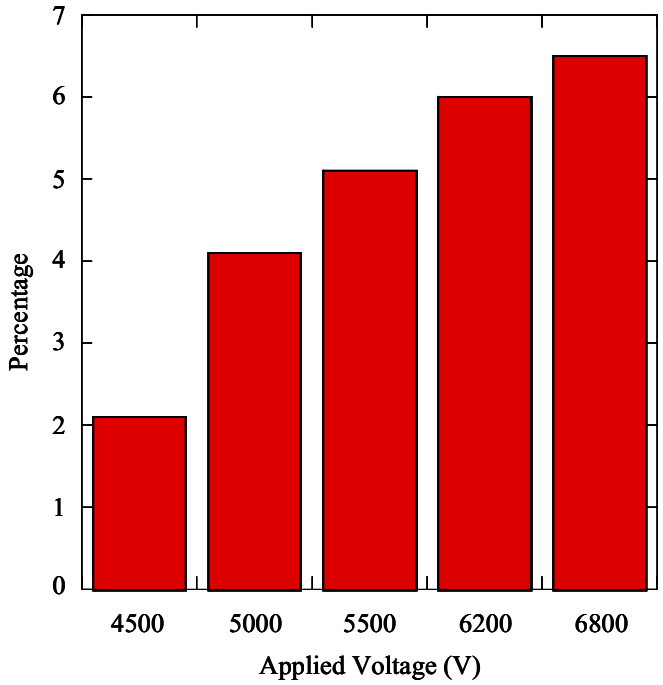

Figure 3.16 Percent speedup until breakdown as a result of using initial conditions.

4. CONCLUSIONS

This thesis addressed the fundamentals needed to model the operation of a metal halide lamp. A complete fluid model has been implemented on an unstructured mesh. This allows the plasma to be modeled accurately while still capturing the geometry of the simulation. Several parameterizations were performed using the completed program yielding logical results.

There were several problems encountered while developing this program that need to be addressed. The biggest problem that needs to be addressed involves a single node that borders the electrode. The electron density at the node typically ends up two orders of magnitude larger than its neighbors. This in turn affects all the other parameters at that node. If the simulation is run long enough, the electron density at the node will eventually diffuse away, but the diffusion coefficient is much too small to allow this to happen as rapidly as the node diverges.

Several possible reasons for this have been speculated upon and pursued. The initial thought was that this problem could be attributed to the boundary conditions between the electrode and the plasma. The boundary conditions used in this simulation assume that all species densities are zero at the electrodes. These may be too simplistic to capture the physics in this region of extremely high electric fields. The boundary conditions were not changed since this would require modification of the solution technique. The second thought was that the rate coefficients for this node were becoming very large due to the large electric fields. Several cases were run to analyze this, and the rates were shown to be exponentially increasing at this node. The results were inconclusive because it was difficult to determine if the large rates were caused by the large *E/N* or as a result of the chemistry diverging. The calculation of the *E/N* is a potential candidate since it is an interpolated variable and is not known with extreme precision.

The chemistry could also be the cause because, at the time, it was solved explicitly. As a result, several different *E/N* interpolation methods were used, and the electron impact reactions were updated to be solved implicitly. Neither of these changes corrected the problem.

Without changing the solution technique, a few more possibilities exist. First, change the solution technique of the chemistry such that all of the reactions are solved fully implicitly. When calculations become stiff, implicit solution techniques tend to converge, while explicit techniques do not. If this does not correct the problem, then the boundary conditions should be modified. The last resort would be to switch from Newton's method to a more stable solution technique.

Another problem that remains to be solved in this program is overlapping cells. Fluid computations rely on the fact that the mesh is conservative. When cells overlap on the mesh, fluxes flowing from one node to the next end up being counted twice. The technique used to discretize the mesh is fine in theory, but when angles on the mesh exceed 90° then the mesh becomes nonconservative. The capability to restrict the angles on the mesh is not an option in the current version of CFD-GEOM. The effect of overlapping cells on the solution of the equations is not known. The appearance of a few hot nodes on the mesh could certainly be attributed to this problem.

Besides the handful of problems that do exist in this program, additional modifications can be made to the program to increase its ability to accurately simulate metal halide lamps. Among the first modifications would be to include a thermal model. The dynamics of the plasma in metal halide lamps are affected dramatically by the thermal gradients that exist. During the cold cathode phase of ignition the mercury that exists on the tip of the electrode is evaporated by high-energy ions, diffuses to the wall, and condenses. Also, later in the ignition

process, thermal emission from the electrode plays a significant role in the development of the steady state arc. If these effects are to be captured by the model, then the large temperature gradients present in the lamp cannot be ignored.

Secondly, the simulations in this thesis do not address the complex chemistries present in metal halide lamps. All the cases simulated in this thesis are 100% argon mixtures; typical doses in lamps include four or five different metals. Although this level of detail requires significant development, simple metals like mercury could be included. This would involve altering the reaction mechanism for the lamp and collecting all of the necessary rate coefficients. The chemistry in the bulk plasma is relatively easy to modify, but the complex surface chemistry that occurs at the wall is difficult. Several states of matter are present, and large thermal gradients exist. A model capturing all these effects would be impressive.

The third addition that will benefit this model is a radiation transport model. Without a radiation transport model, it is difficult to quantify the lamp's efficiency and predict the effect of one parameter. This addition would obviously have to follow the update of the chemistry since the doses in the lamp determine the color and efficiency.

Finally, a means to simulate the external UV starter would be beneficial. The UV starter has a significant impact on the ignition process of the lamp. Although it is computationally expensive to include the starter in the mesh, it would be appropriate to introduce a random variable that would determine ionizations due to the UV starter. It would be interesting to see how this would affect the simulations.

The model implemented for this thesis captures the fundamental physics involved in the metal halide lamp and forms the basis of a more complex simulation.